

APRIL 22 2024

## Paraxial and ray approximations of acoustic vortex beams

Chirag A. Gokani; Michael R. Haberman  ; Mark F. Hamilton 

 Check for updates

*J. Acoust. Soc. Am.* 155, 2707–2723 (2024)

<https://doi.org/10.1121/10.0025688>

  
View  
Online

  
Export  
Citation



ASA

LEARN MORE

Advance your science and career as a member of the  
**Acoustical Society of America**

# Paraxial and ray approximations of acoustic vortex beams

Chirag A. Gokani,<sup>1,2</sup> Michael R. Haberman,<sup>1,2</sup>  and Mark F. Hamilton<sup>1,2,a)</sup> 

<sup>1</sup>Applied Research Laboratories, The University of Texas at Austin, Austin, Texas 78766-9767, USA

<sup>2</sup>Walker Department of Mechanical Engineering, The University of Texas at Austin, Austin, Texas 78712-1063, USA

## ABSTRACT:

A compact analytical solution obtained in the paraxial approximation is used to investigate focused and unfocused vortex beams radiated by a source with a Gaussian amplitude distribution. Comparisons with solutions of the Helmholtz equation are conducted to determine bounds on the parameter space in which the paraxial approximation is accurate. A linear relation is obtained for the dependence of the vortex ring radius on the topological charge, characterized by its orbital number, in the far field of an unfocused beam and in the focal plane of a focused beam. For a focused beam, it is shown that as the orbital number increases, the vortex ring not only increases in radius but also moves out of the focal plane in the direction of the source. For certain parameters, it is demonstrated that with increasing orbital number, the maximum amplitude in a focused beam becomes localized along a spheroidal surface enclosing a shadow zone in the prefocal region. This field structure is described analytically by ray theory developed in the present work, showing that the spheroidal surface in the prefocal region coincides with a simple expression for the coordinates of the caustic surface formed in a focused vortex beam. © 2024 Acoustical Society of America.

<https://doi.org/10.1121/10.0025688>

(Received 19 January 2024; revised 27 March 2024; accepted 27 March 2024; published online 22 April 2024)

[Editor: Philip L. Marston]

Pages: 2707–2723

## I. INTRODUCTION

Vortex beams have been studied in optics for over three decades, starting with the observation by Allen *et al.*<sup>1</sup> that eigenfunctions used in paraxial optics possess orbital angular momentum proportional to the orbital number  $\ell$ , also known as the azimuthal index or topological charge. Optical vortices have since been studied intensely, leading to their application to particle manipulation using optical tweezers and communication devices with high data rates.<sup>2</sup> Interest in optical vortices began with the study by Coullet *et al.*,<sup>3</sup> who demonstrated the existence of vortex states of light in a laser cavity through a numerical study of the Maxwell-Bloch equations. Coullet *et al.* were inspired by hydrodynamic vortex rings, which were first studied by Helmholtz.<sup>4</sup> The study of vortices returned to fluid mechanics, not as the traditional incompressible rotation of a fluid but as an acoustic wave phenomenon, with Hefner and Marston's<sup>5</sup> numerical and experimental demonstration of an underwater acoustic vortex beam. Analogous to their optical counterparts, acoustic vortex beams have since been applied to particle manipulation<sup>6–13</sup> and acoustic communication.<sup>14–20</sup> They have also been applied in biomedical ultrasound<sup>21–23</sup> and have even been used to create sound-diffusing surfaces.<sup>24</sup> An extensive review of the generation and application of acoustic vortex beams was published recently by Guo *et al.*<sup>25</sup>

The generation of acoustic vortex beams remains a central challenge to their use. A straightforward approach is to use arrays of acoustic transducers with the necessary

phasing and amplitude shading with<sup>26</sup> or without<sup>13,27</sup> focusing lenses. While the use of arrays of active elements has the advantage of being adaptable to different scenarios, they require multiple electroacoustic channels with their associated hardware and algorithms to generate the desired field.<sup>13</sup> Alternative single-channel approaches include the use of a wrapped transducer geometry as shown by Baudoin *et al.*,<sup>11</sup> or a helicoidal transducer shape that introduces the necessary angle-dependent phase gradient at the radiating surface as first shown by Hefner and Marston.<sup>5</sup> The latter examples were precursors to more recent efforts to design conventional or metamaterial lenses to introduce the helicoidal and focusing phase so that one may use a single-channel source that has a uniformly phased aperture.<sup>28–32</sup> Metamaterial examples include the use of side-branch Helmholtz resonators<sup>33,34</sup> or labyrinthine structures to generate acoustic vortices in air.<sup>35,36</sup> Other unique approaches include using arrays of helicoids,<sup>37</sup> circular gratings to create a leaky wave antenna,<sup>38,39</sup> and the generation of vortices in reflected sound fields by designing grooves in a reflective surface.<sup>40</sup> Adaptation of metamaterial structures designed for airborne acoustics has been extended to underwater acoustics, with examples including two sets of Archimedian spirals,<sup>31</sup> porous rubber layers with spatially graded subwavelength structure,<sup>30</sup> and pentamode lattice structures<sup>19</sup> similar to previous work on planar underwater pentamode lenses.<sup>41,42</sup>

The design of conventional or metamaterial vortex sources requires accurate and efficient analytical or numerical models to calculate the field, similar to how the design of focused sources could be informed by the O'Neil model<sup>43</sup> prior to development of more computationally expensive

<sup>a)</sup>Email: hamilton@mail.utexas.edu

numerical models. A common approach to modeling vortex beams employs the superposition of Laguerre-Gaussian modes, which are solutions of the paraxial approximation of the Helmholtz equation in cylindrical coordinates.<sup>44</sup> Because these modes form a complete orthogonal set, they can be used to describe directional radiation from a source plane with any amplitude and phase distribution that satisfies the restrictions on the paraxial approximation.

In the present work the Fresnel diffraction integral is used, which is also a solution of the paraxial approximation of the Helmholtz equation. The advantage of this approach is the simplicity of the analytical solution obtained for the case of a vortex beam radiated by a source with a Gaussian amplitude distribution, either focused or unfocused. This approach facilitates rapid iterations when designing radiating surfaces and provides physical insights that can be obscured when using Laguerre-Gaussian modes. The solution presented here consists of a compact analytical expression, whereas it is shown in the Appendix that an infinite series is required to describe the same beam using the Laguerre-Gauss expansion.

Another benefit of the analytical solution obtained from the Fresnel diffraction integral is that the amplitude distribution in the source plane is unaltered by changes in the orbital number  $\ell$ , permitting the consequences of varying  $\ell$  to be decoupled from variations in other source parameters. In contrast, changing the value of  $\ell$  for a field described by a single Laguerre-Gaussian mode alters the amplitude distribution corresponding to that mode in the source plane. Decoupling the source amplitude from the value of  $\ell$  is also relevant to configurations in which a single source is employed and  $\ell$  is changed by inserting a different phase screen in front of that source, as in the experiments with focused acoustic vortex beams reported by Terzi *et al.*<sup>29</sup>

The analytical solution based on the paraxial approximation for a focused or unfocused vortex beam radiated from a planar source with a Gaussian amplitude distribution is obtained in Sec. II. Similar solutions were derived previously in optics, one for unfocused vortex beams by Kotlyar *et al.*<sup>45</sup> and another for focused vortex beams by Sacks *et al.*<sup>46</sup> but which is restricted to the focal plane. In Sec. III, it is shown that the analytical solution yields a linear dependence on  $\ell$  for the radius of the vortex ring in the far field of an unfocused beam and in the focal plane of a focused beam.

In Sec. IV, a simple criterion is obtained for the parameter space in which solutions based on the paraxial approximation for unfocused vortex beams are accurate, which is confirmed by comparisons with solutions of the Helmholtz equation. A similar comparison is reported in Sec. V for focused beams, but the additional complexity introduced by focusing precludes derivation of an analytical criterion. Instead, regions of the parameter space in which the paraxial approximation was found to be accurate for focused beams are presented as decision matrices.

Most notable in Sec. V is a demonstration that as  $\ell$  is increased, the vortex ring moves out of the focal plane in the

direction of the source. Under certain conditions, the vortex ring becomes redistributed along a surface that encloses a shadow zone in the prefocal region. These features motivated development of the ray theory in Sec. VI, which yields an analytical expression for the coordinates of the caustic surfaces in vortex beams. In focused vortex beams, the caustic surface in the prefocal region is a spheroid that encloses the shadow zone predicted by diffraction theory. A related wave phenomenon, referred to as an autofocusing vortex beam, has been observed in optics and modeled with caustics predicted by ray theory.<sup>47</sup> Distinctions between autofocusing vortex beams and the vortex beams modeled in the present work are drawn following the discussion of Fig. 8 below.

## II. ANALYTICAL SOLUTION IN THE PARAXIAL APPROXIMATION

An acoustic pressure field  $p$  expressed with time dependence  $e^{-i\omega t}$  suppressed is a solution of the Helmholtz equation,

$$\nabla^2 p + k^2 p = 0, \quad (1)$$

where  $k = \omega/c_0$  is the wavenumber and  $c_0$  is the sound speed in the fluid. For narrow beams propagating along the  $z$  axis and described by  $p = qe^{ikz}$ , where  $q$  is a function that varies sufficiently slowly with  $z$  that  $|\partial^2 q/\partial z^2| \ll 2k|\partial q/\partial z|$ , Eq. (1) may be replaced by what is commonly referred to as its paraxial approximation:

$$2ik \frac{\partial q}{\partial z} + \nabla_{\perp}^2 q = 0. \quad (2)$$

The operator  $\nabla_{\perp}^2$  is the Laplacian in the plane perpendicular to the  $z$  axis, given by  $\partial^2/\partial x^2 + \partial^2/\partial y^2$  in Cartesian coordinates. The solution of Eq. (2) may be expressed in Cartesian coordinates as the Fresnel diffraction integral:

$$q(x,y,z) = -\frac{ik}{2\pi z} \int \int_{-\infty}^{\infty} q(x_0, y_0, 0) e^{i(k/2z)[(x-x_0)^2 + (y-y_0)^2]} dx_0 dy_0, \quad (3)$$

where  $q(x,y,0)$  is the source condition for the sound pressure in the plane  $z=0$ . Consistent with the paraxial approximation, the pressure source condition  $q(x,y,0)$  may be replaced by the  $z$  component of the particle velocity in the source plane multiplied by  $\rho_0 c_0$ , where  $\rho_0$  is the density of the fluid.<sup>48</sup>

The source condition for a focused vortex beam with a Gaussian amplitude distribution in the plane  $z=0$  is more conveniently expressed in cylindrical coordinates  $(r, \theta, z)$ :

$$q(r, \theta, 0) = p_0 e^{-r^2/a^2} e^{-ikr^2/2d} e^{i\ell\theta}, \quad (4)$$

where  $p_0$  is the peak acoustic pressure at the origin,  $a$  is the Gaussian source radius,  $d$  is the geometric focal length, and  $\ell$  is the orbital number. The corresponding source condition

for an unfocused vortex beam is obtained by setting  $d = \infty$ . For convenience, it is assumed in the present work that  $\ell$  is non-negative ( $\ell = 0, 1, 2, \dots$ ), recognizing that the magnitude of the resulting complex pressure field is unaltered by changing the sign of  $\ell$ , and the effect on the phase is only to reverse the helical polarity (sometimes referred to as handedness) of the wavefronts. Since the time-averaged intensity radiated by the source is  $I = |q(r, \theta, 0)|^2 / 2\rho_0 c_0$  in the paraxial approximation, the corresponding time-averaged power radiated by the source is

$$\mathcal{P}_0 = \frac{1}{2\rho_0 c_0} \int_0^{2\pi} \int_0^\infty |q(r, \theta, 0)|^2 r dr d\theta = \frac{\pi a^2 p_0^2}{4\rho_0 c_0}, \quad (5)$$

which is independent of  $\ell$ .

Conversion of Eq. (3) to cylindrical coordinates yields

$$q(r, \theta, z) = -\frac{ik}{2\pi z} \int_0^{2\pi} \int_0^\infty q(r_0, \theta_0, 0) e^{i(k/2z)[r^2 + r_0^2 - 2rr_0 \cos(\theta_0 - \theta)]} r_0 dr_0 d\theta_0 \quad (6)$$

for the Fresnel diffraction integral, and following substitution of Eq. (4) for the source condition one obtains

$$q(r, \theta, z) = -\frac{ikp_0}{2\pi z} e^{ikr^2/2z} \int_0^\infty e^{-r_0^2/a^2} e^{i(kr_0^2/2)(z^{-1}-d^{-1})} r_0 dr_0 \times \int_0^{2\pi} e^{i\ell\theta_0} e^{-i(krr_0/z) \cos(\theta_0 - \theta)} d\theta_0 \quad (7)$$

for the field of the focused vortex beam in the paraxial approximation. Making the variable substitution  $\theta_0 = \phi - \pi/2 + \theta$  in Eq. (7) in order to convert  $\cos(\theta_0 - \theta)$  to  $\sin\phi$ , and then employing Watson's relation<sup>49</sup>

$$J_n(\beta) = \frac{1}{2\pi} \int_{-\alpha}^{2\pi+\alpha} e^{i(n\phi - \beta \sin\phi)} d\phi, \quad (8)$$

where  $J_n$  is the Bessel function of the first kind of order  $n$  and  $\alpha$  is an arbitrary constant, yields

$$\int_0^{2\pi} e^{i\ell\theta_0} e^{-i(krr_0/z) \cos(\theta_0 - \theta)} d\theta_0 = 2\pi e^{i\ell(\theta - \pi/2)} J_\ell(krr_0/z). \quad (9)$$

The solution thus reduces to

$$q(r, \theta, z) = -ikp_0 \frac{e^{ikr^2/2z}}{z} e^{i\ell(\theta - \pi/2)} \times \int_0^\infty e^{-[1-i(ka^2/2z)(1-z/d)]r_0^2/a^2} J_\ell(krr_0/z) r_0 dr_0, \quad (10)$$

in which the coefficients of  $r_0^2$  have been grouped together in preparation for the remaining integration.

The integral over  $r_0$  may be evaluated with the relation<sup>50</sup>

$$\begin{aligned} \int_0^\infty xe^{-\alpha x^2} J_n(\beta x) dx &= \frac{\sqrt{\pi}\beta}{8\alpha^{3/2}} \exp\left(-\frac{\beta^2}{8\alpha}\right) \\ &\times \left[ I_{(n-1)/2}\left(\frac{\beta^2}{8\alpha}\right) - I_{(n+1)/2}\left(\frac{\beta^2}{8\alpha}\right) \right], \end{aligned} \quad (11)$$

where  $I_\nu(\chi) = i^{-\nu} J_\nu(i\chi)$  is the modified Bessel function of the first kind of order  $\nu$ . The stated restrictions on Eq. (11) are  $\text{Re } \alpha > 0$  and  $n > -2$ , which are satisfied in the present work.

Use of Eq. (11) to evaluate Eq. (10) yields the following analytical solution in the paraxial approximation for a focused vortex beam radiated by a source with a Gaussian amplitude distribution:

$$q(r, \theta, z) = \sqrt{8\pi} \frac{p_0 z}{kr^2} \chi^{3/2} e^{-\chi} [I_{(\ell-1)/2}(\chi) - I_{(\ell+1)/2}(\chi)] \times e^{i[\ell\theta - (\ell+1)\pi/2 + kr^2/2z]}, \quad (12)$$

where

$$\chi(r, z) = \frac{\frac{1}{8}(kar/z)^2}{1 - i(ka^2/2z)(1 - z/d)}. \quad (13)$$

The magnitude of Eq. (12) is

$$|q(r, z)| = \sqrt{8\pi} \frac{p_0 z}{kr^2} |\chi^{3/2} e^{-\chi} [I_{(\ell-1)/2}(\chi) - I_{(\ell+1)/2}(\chi)]|, \quad (14)$$

which is independent of  $\theta$ . It can be shown by integrating  $|q(r, z)|^2$  numerically over any plane for which  $z = \text{const}$  that the source power  $\mathcal{P}_0$  in Eq. (5) is recovered independent of  $\ell$ . The solution for an unfocused source is obtained by setting  $d = \infty$  in Eq. (13).

A solution in the general form of Eq. (12) was obtained previously in optics by Kotlyar *et al.*<sup>45</sup> for an unfocused vortex beam ( $d = \infty$ ), although their solution is expressed less compactly in terms of the notation employed in the Appendix of the present work. For the case of a focused vortex beam, evaluation of Eq. (12) in the focal plane ( $z = d$ ) recovers the corresponding result obtained in optics by Sacks *et al.*<sup>46</sup>

The present section concludes with two limiting forms of Eq. (12). For  $\ell = 0$  (no vorticity), the traditional solution for a focused Gaussian beam is recovered:<sup>51</sup>

$$q(r, z) = \frac{p_0}{1 - (1 - iG^{-1})z/d} \times \exp\left(-\frac{(1 + iG)r^2/a^2}{1 - (1 - iG^{-1})z/d}\right), \quad \ell = 0, \quad (15)$$

where  $G = ka^2/2d$  is the gain at the geometric focus,  $(r, z) = (0, d)$ . Equation (15) follows from Eq. (12) via the relation<sup>52</sup>

TABLE I. The roots  $\chi_\ell$  of Eq. (21) and the corresponding coefficients  $\eta_\ell$  for  $1 \leq \ell \leq 10$ .

$\ell$	1	2	3	4	5	6	7	8	9	10
$\chi_\ell$	0.3564	0.8966	1.6177	2.5357	3.6718	5.0436	6.6614	8.5294	10.6489	13.0196
$\eta_\ell = \sqrt{8\chi_\ell}$	1.6885	2.6783	3.5974	4.5040	5.4198	6.3521	7.3001	8.2605	9.2299	10.2057

$$I_{-1/2}(\chi) - I_{1/2}(\chi) = -\sqrt{2\chi/\pi} h_0^{(1)}(i\chi) = \sqrt{2/\pi} \frac{e^{-\chi}}{\sqrt{\chi}}, \quad (16)$$

where  $h_0^{(1)}$  is the spherical Hankel function of the first kind of order zero. The beam profile perpendicular to the  $z$  axis is Gaussian at all distances. In the focal plane one obtains  $|q(r, d)| = Gp_0 e^{-r^2/(a/G)^2}$ , indicating that the amplitude is increased, and the beamwidth is decreased, by the factor  $G$ . For an unfocused source ( $d = \infty$ ), Eq. (15) reduces to

$$q(r, z) = \frac{p_0}{1 + iz/z_R} \exp\left(-\frac{r^2/a^2}{1 + iz/z_R}\right), \\ \ell = 0, \quad d = \infty, \quad (17)$$

where  $z_R = ka^2/2$  is the Rayleigh distance.

A common alternative approach to describing vortex beams in the paraxial approximation is the Laguerre-Gauss expansion. The coefficients in this expansion are calculated analytically in the Appendix for an unfocused beam, the source condition for which is Eq. (4) with  $d = \infty$ , and the results are compared with the solution given by Eq. (12).

### III. VORTEX RING RADIUS

For  $\ell > 0$ , the radiated field does not possess a Gaussian beam profile perpendicular to the  $z$  axis as described by Eqs. (15) and (17) for  $\ell = 0$ , and instead the pressure field is zero along the  $z$  axis. A traditional descriptor of a vortex beam is therefore the radius (distance from the  $z$  axis) of the resulting vortex ring where the amplitude defined by Eq. (14) is maximized in a plane perpendicular to the  $z$  axis.

Calculation of the vortex ring radius, or spot size, is accomplished most easily when  $\chi$  in Eq. (13) is a real quantity, which occurs for two cases of practical interest, in the focal plane of a focused beam ( $z = d$ ) and in the far field of an unfocused beam ( $d = \infty, z \gg z_R$ ):

$$\chi = \frac{1}{8}(kar/d)^2, \quad z = d, \quad (18)$$

$$= \frac{1}{8}(kar/z)^2, \quad d = \infty, \quad z \gg z_R. \quad (19)$$

The locations of the amplitude maxima described by Eq. (14) in the plane of interest perpendicular to the  $z$  axis are determined by setting  $\partial|q|/\partial r = 0$ , which for the cases defined by Eqs. (18) and (19) are equivalent to satisfying the relation

$$\frac{d}{d\chi} \left\{ \chi^{1/2} e^{-\chi} [I_{(\ell-1)/2}(\chi) - I_{(\ell+1)/2}(\chi)] \right\} = 0. \quad (20)$$

Taking the derivative yields

$$(\ell - 4\chi)I_{(\ell-1)/2}(\chi) + (\ell + 4\chi)I_{(\ell+1)/2}(\chi) = 0, \quad (21)$$

which is the relation obtained by Kotlyar *et al.*<sup>45</sup> for the far-field case in Eq. (19), the root of which they present only for  $\ell = 2$ .

Here, Eq. (21) is solved numerically for the single root  $\chi_\ell$  corresponding to each orbital number. In the absence of vorticity ( $\ell = 0$ ), Eq. (21) yields  $\chi_0 = 0$ , as required for the fields described by Eqs. (15) and (17), whose amplitudes decrease monotonically with distance from the  $z$  axis. The roots  $\chi_\ell$  for  $1 \leq \ell \leq 10$  are presented in Table I. The ring radii determined by Eqs. (18) and (19) are expressed as

$$r_\ell = \eta_\ell d/ka, \quad z = d, \quad (22)$$

$$= \eta_\ell z/ka, \quad d = \infty, \quad z \gg z_R, \quad (23)$$

where the values of  $\eta_\ell = \sqrt{8\chi_\ell}$  are also presented in Table I. An alternative form of Eq. (23) is  $\psi_\ell = \arctan(\eta_\ell/ka)$ , where  $\psi_\ell$  is the angle with respect to the  $z$  axis of the maximum in the far field, defined by  $\tan \psi_\ell = r_\ell/z$ .

A least squares fit of the values in the bottom row of Table I over the range  $1 \leq \ell \leq 10$  yields the linear relation

$$\eta_\ell = 0.9405\ell + 0.7518, \quad (24)$$

with a correlation coefficient of 0.999. Comparison of the values  $\eta_\ell$  in Table I with Eq. (24) is presented in Fig. 1. A linear dependence on  $\ell$  was also obtained by Curtis and Grier<sup>53</sup> for the ring radius in the focal plane of an optical vortex beam with uniform amplitude in the source plane. However, as discussed in Sec. V, the global maximum predicted by Eq. (14) moves away from the plane  $z = d$  with increasing  $\ell$ . Therefore, while Eq. (22) provides an accurate prediction of the ring radius corresponding to the global

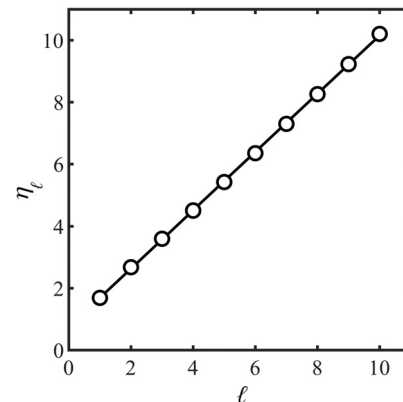


FIG. 1. Comparison of the values  $\eta_\ell$  in Table I (circles) with the least squares fit given by Eq. (24) (line).

maximum in a focused vortex beam with a low orbital number, its accuracy in this context decreases as  $\ell$  increases.

#### IV. PARAXIAL APPROXIMATION OF UNFOCUSSED VORTEX BEAMS

Limitations on Eq. (12) that arise from the paraxial approximation associated with Eq. (2) may be identified via comparison with solutions of the Helmholtz equation, Eq. (1), that satisfy the same source condition, Eq. (4). The solutions of Eq. (1) used for comparison in the present section were obtained numerically using spatial Fourier transforms.

The paraxial approximation underlying the slow variation in  $q$  as a function of  $z$  that leads to Eq. (2) is based on the assumption that the radiated field is formed by waves propagating in directions forming small angles with the  $z$  axis.<sup>54</sup> As  $\ell$  increases, these angles increase, and the paraxial approximation becomes increasingly inaccurate. This feature of the field is characterized by its angular spectrum, which is obtained by taking the spatial Fourier transform of the source function.

The following definitions of the 2D spatial Fourier transform and its inverse are employed for solving the Helmholtz equation:

$$\mathcal{F}_{2D}\{f\} = \hat{f}(k_x, k_y) = \int \int_{-\infty}^{\infty} f(x, y) e^{-i(k_x x + k_y y)} dx dy, \quad (25)$$

$$f(x, y) = \mathcal{F}_{2D}^{-1}\{\hat{f}\} = \frac{1}{4\pi^2} \int \int_{-\infty}^{\infty} \hat{f}(k_x, k_y) e^{i(k_x x + k_y y)} dk_x dk_y. \quad (26)$$

For a source described by a pressure field in the plane  $z=0$ , the solution of Eq. (1) may be expressed as<sup>55</sup>

$$p_H(x, y, z) = \mathcal{F}_{2D}^{-1}\{e^{ik_z z} \mathcal{F}_{2D}[p_H(x, y, 0)]\}, \quad (27)$$

where  $k_z = (k^2 - k_x^2 - k_y^2)^{1/2}$ . The subscript  $H$  is introduced to distinguish the solution of the Helmholtz equation from its paraxial approximation, with  $p_H(x, y, 0) = q(x, y, 0)$  in the source plane. Conversion of Eq. (4) to Cartesian coordinates yields

$$p_H(x, y, 0) = p_0 e^{-(x^2 + y^2)/a^2} e^{-ik(x^2 + y^2)/2d} e^{i\ell \arctan(x, y)} \quad (28)$$

for the source function used in Eq. (27). In its numerical implementation, the function  $\arctan$  is evaluated using  $\text{atan2}(y, x)$  to determine the phase angle throughout the range  $-\pi < \theta \leq \pi$ .

It is instructive to examine first the angular spectrum of the source function. To obtain an analytical expression for its angular spectrum, the following polar form of Eq. (25) with  $k_x = \kappa \cos \phi$  and  $k_y = \kappa \sin \phi$  is used:

$$\hat{f}(\kappa, \phi) = \int_0^{2\pi} \int_0^{\infty} f(r, \theta) e^{-ikr \cos(\theta - \phi)} r dr d\theta, \quad (29)$$

where  $\kappa = (k_x^2 + k_y^2)^{1/2}$  and  $\phi = \arctan(k_y/k_x)$ . Throughout the remainder of the present section, we consider the source condition in Eq. (4) without focusing, i.e., with  $d = \infty$ :

$$q(r, \theta, 0) = p_0 e^{-r^2/a^2} e^{i\ell\theta}, \quad d = \infty. \quad (30)$$

Note that the focused source condition in Eq. (4) is recovered by replacing  $a^2$  in Eq. (30) with the complex quantity  $\tilde{a}^2 = a^2/(1 + ika^2/2d)$ , a transformation that will be used in Sec. V. Substitution of Eq. (30) in Eq. (29) and making use of Eqs. (8) and (11) as before yields for the angular spectrum of the unfocused Gaussian vortex source

$$\begin{aligned} \hat{q}(\kappa, \phi, 0) &= a^2 p_0 \frac{\pi^{3/2}}{\sqrt{2}} \Omega^{1/2} e^{-\Omega} \\ &\times [I_{(\ell-1)/2}(\Omega) - I_{(\ell+1)/2}(\Omega)] e^{i\ell(\phi - \pi/2)}, \\ &d = \infty, \end{aligned} \quad (31)$$

$$\text{where } \Omega = \frac{1}{8}(\kappa a)^2.$$

Since Eq. (31) has the same form as Eq. (12), the location of the peak in the angular spectrum determined by setting  $d|\hat{q}|/d\Omega = 0$  yields  $\Omega = \chi_\ell$ , where  $\chi_\ell$  is the root of Eq. (21). Making use of the relation  $\chi_\ell = \frac{1}{8}\eta_\ell^2$  employed in Eqs. (22) and (23), one obtains  $\kappa_\ell = \eta_\ell/a$  for the value of  $\kappa$  where the peak in the angular spectrum occurs, which increases linearly with  $\ell$  according to Eq. (24) and Fig. 1. For  $\ell$  sufficiently large that  $\kappa_\ell > k$ , in which case  $k_z = (k^2 - \kappa^2)^{1/2}$  in Eq. (27) is imaginary for  $\kappa \simeq \kappa_\ell$ , the plane waves in the angular spectrum forming the vortex ring defined by Eq. (23) are evanescent. Evanescent waves are not described by the paraxial approximation, which corresponds to replacing  $k_z$  by  $k - \kappa^2/2k$  in Eq. (27),<sup>54</sup> requiring  $\kappa^2 \ll k^2$  for this approximation to be accurate. Therefore, the paraxial approximation should provide an accurate description of the ring that characterizes a vortex beam only for

$$k^2 \gg \kappa_\ell^2, \quad (32)$$

which for Eq. (12) in the absence of focusing corresponds to  $(ka)^2 \gg \eta_\ell^2$ , or alternatively

$$(ka)^2 \gg \ell^2, \quad d = \infty, \quad (33)$$

based on the values of  $\eta_\ell$  in the lower row of Table I. This result is consistent with the statement preceding the paraxial approximation in Eq. (2) that  $q$  is a slowly varying function of  $z$ .

To assess the validity of the condition in Eq. (33) for determining the parameter space in which the paraxial approximation accurately describes the vortex ring radiated by the unfocused source defined by Eq. (30), presented in Fig. 2 is a comparison of Eq. (14) (red curves) in the absence of focusing ( $d = \infty$ ) with the magnitudes of the solutions of the Helmholtz equation (blue curves) obtained numerically from Eq. (27). All beam profiles were calculated at the same distance from the source plane,  $z/z_R = 1$ , where  $z_R = ka^2/2$  is again the Rayleigh distance. The columns in Fig. 2 correspond to different values of  $\ell$  increasing from 1 to 10, and the values of  $ka$  for the rows were chosen to be 3 times the values of  $\ell$  used for

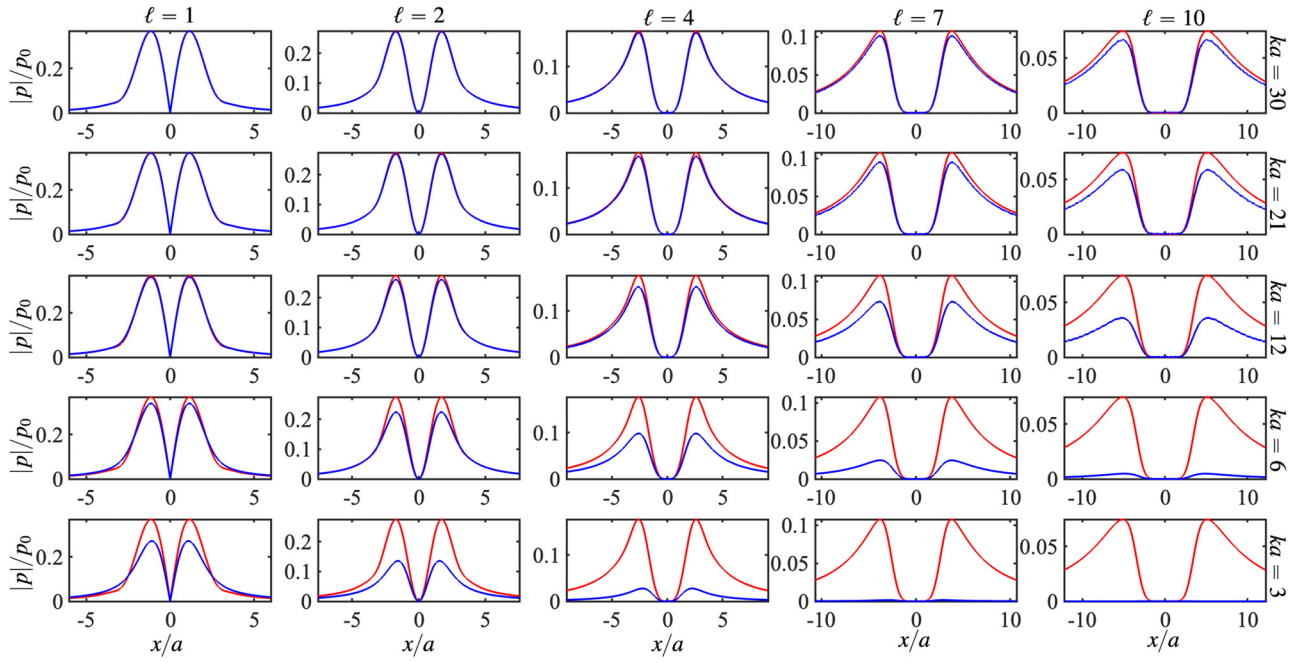


FIG. 2. (Color online) Comparison of Eq. (14) (red curves) for the unfocused source condition in Eq. (30) with solutions of the Helmholtz equation (blue curves) obtained numerically from Eq. (27) at  $z = z_R$ , where  $z_R = k^2/2$  is the Rayleigh distance. The relation  $ka = 3\ell$  applies to each plot that lies along the diagonal extending from the lower left to upper right corner, with  $ka > 3\ell$  for each plot above the diagonal and  $ka < 3\ell$  for each plot below the diagonal.

the columns. In this way, the relation  $ka = 3\ell$  applies to each plot that lies along the diagonal extending from the lower left to upper right corner of Fig. 2. It is observed that above the diagonal, where  $ka > 3\ell$  for each plot, the paraxial approximation is in good agreement with the solution of the Helmholtz equation, and below the diagonal, where  $ka < 3\ell$  for each plot, there is noticeable disagreement that increases with  $\ell$  for any fixed value of  $ka$ . Comparisons at distances  $z/z_R = 0.5$  and  $z/z_R = 2$  look much the same. Since  $(ka)^2 = 9\ell^2$  applies to all plots along the diagonal of Fig. 2, the relation

$$ka > 3\ell, \quad d = \infty \quad (34)$$

is consistent with the criterion in Eq. (33) for the paraxial approximation to accurately describe an unfocused vortex beam with Gaussian amplitude distribution in the source plane for  $\ell \leq 10$ .

It is reasonable to check whether the criterion in Eq. (33) is suitable for vortex beams with source amplitudes other than Gaussian, and this is easily done using Eq. (27) to solve not only the Helmholtz equation, Eq. (1), but also its paraxial approximation, Eq. (2). The latter is accomplished by replacing  $p_H$  with  $q$  and  $k_z = (k^2 - k_x^2 - k_y^2)^{1/2}$  with  $k_z = k - (k_x^2 + k_y^2)/2k$  in Eq. (27). In place of Eq. (30), the unfocused source condition considered here has uniform pressure amplitude within a circle of radius  $a$  and zero amplitude outside that circle:

$$q(r, \theta, 0) = p_0 \text{circ}(r/a) e^{i\ell\theta}, \quad (35)$$

where the circle function  $\text{circ } \alpha$  is unity for  $\alpha \leq 1$  and zero for  $\alpha > 1$ . Solutions of Eqs. (1) and (2) for the source

function in Eq. (35) are compared in Fig. 3, which has the same format as Fig. 2 except with  $ka = 4\ell$  for the plots along the diagonal. The agreement above the diagonal, where  $ka > 4\ell$  for each plot, is not quite as good as above the diagonal in Fig. 2, but the differences are mainly in the sidelobes outside the vortex ring. Equation (33) is thus observed to also be a reasonable criterion for use of the paraxial approximation to describe the vortex rings in fields corresponding to the unfocused source function in Eq. (35), at least for  $\ell \leq 10$ .

The reader is referred to Zhang and Marston<sup>6</sup> for discussion of modeling angular momentum flux in acoustic vortex beams with and without use of the paraxial approximation.

## V. PARAXIAL APPROXIMATION OF FOCUSED VORTEX BEAMS

The approach used in Sec. IV to assess the validity of the paraxial approximation applies to focused vortex beams as well. Inclusion of focusing in Eq. (31) for the angular spectrum is straightforward. As noted following Eq. (30), Eq. (4) is recovered by replacing  $a^2$  in Eq. (30) with the complex quantity  $\tilde{a}^2 = a^2/(1+iG)$ , where  $G = ka^2/2d$ . Focusing is therefore included in Eq. (31) by multiplying the expression by  $(1+iG)^{-1}$  and replacing the quantity  $\Omega$  with  $\tilde{\Omega} = \frac{1}{8}(\kappa a)^2/(1+iG)$ . Since  $\hat{q}$  is then a function of the complex quantity  $\tilde{\Omega}$ , the roots of Eq. (21) no longer determine the values of  $\kappa_\ell$  associated with the peaks in the angular spectra.

Presented in Fig. 4(a) are the values of  $\kappa_\ell a$  corresponding to the maximum value in the magnitude of the angular spectrum  $|\hat{q}(ka)|$  calculated numerically for  $1 \leq \ell \leq 10$  with

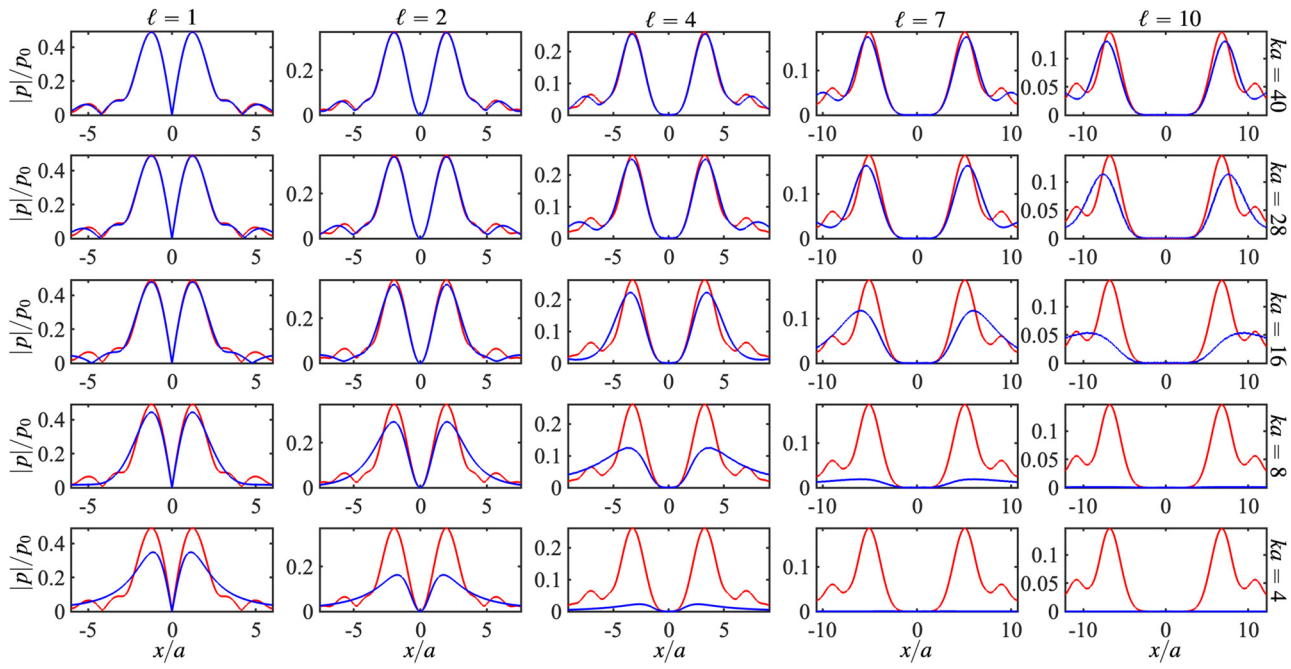


FIG. 3. (Color online) Comparison of the paraxial approximation (red curves) with the solution of the Helmholtz equation (blue curves) at  $z = z_R$  as in Fig. 2 but for the unfocused uniform circular source condition in Eq. (35). The paraxial approximation in this case is obtained numerically from Eq. (27) with  $k_z$  replaced by  $k - (k_x^2 + k_y^2)/2k$ . The relation  $ka = 4\ell$  applies to each plot along the diagonal, with  $ka > 4\ell$  for each plot above the diagonal and  $ka < 4\ell$  for each plot below the diagonal.

values of  $G$  increasing in order from  $G=0$  (bottom curve) to  $G=80$  (top curve). In contrast with the unfocused vortex beam ( $G=0$ ), the dependence on  $\ell$  is no longer linear for  $G>0$ , and the departure from a linear dependence increases with  $G$ . Also, it follows from the relation  $(ka)^2 = 8(1+iG)\tilde{\Omega}$  that  $ka \simeq (8iG\tilde{\Omega})^{1/2}$  for  $G^2 \gg 1$ , and it may be observed that for  $G>0$  the curves for different values of  $G$  in Fig. 4(a) increase relative to one another approximately in proportion to  $G^{1/2}$ . As for unfocused vortex beams, the criterion for the validity of the paraxial approximation in the case of focused vortex beams is given by Eq. (32),  $k^2 \gg \kappa_\ell^2$ . However, the dependence of  $\kappa_\ell a$  on  $\ell$  and  $G$  observed in Fig. 4(a) does not lend itself to formulation of a simple explicit criterion such as Eq. (33) for unfocused vortex beams.

Further insight into the difficulty with determining a simple criterion for the accuracy of the paraxial approximation used for focused vortex beams is provided by the magnitudes of the angular spectra presented in Figs. 4(b)–4(d) for  $G=0, 10$ , and  $40$ , respectively, with  $\ell=1, 5$ , and  $10$  for each value of  $G$ . Whereas the spectra in Fig. 4(b) for unfocused beams ( $G=0$ ) possess no oscillations, the spectra in the lower row of Fig. 4 not only reveal pronounced oscillations, but also increased spatial bandwidth, associated with focusing ( $G>0$ ).

A parametric study similar to those in Figs. 2 and 3, in which the fields radiated by unfocused sources calculated with solutions of the Helmholtz equation and their paraxial approximations are compared as functions of  $ka$  and  $\ell$ , was performed for focused sources, which introduces the additional parameter  $d/a$ . For reference, it should be noted that

$ka$  and  $d/a$  are related to the quantity  $G$  in Fig. 4 by their ratio  $ka/(d/a) = 2G$ . The comparisons for focused beams employ the source conditions in Eqs. (4) and (35) for Gaussian and uniform amplitude distributions, respectively,

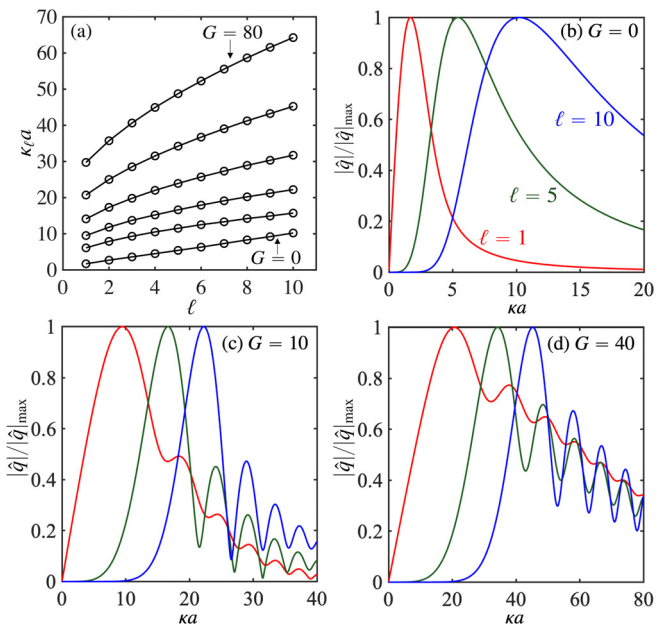


FIG. 4. (Color online) (a) Values of  $\kappa_\ell a$  for selected values of  $\ell$  and  $G = ka^2/2d$ , with the curves for  $G=0, 5, 10, 20, 40$ , and  $80$  displayed with  $G$  increasing from bottom to top, corresponding to the maximum value in the magnitude of the angular spectrum described by Eq. (31) following modification for application to a focused vortex beam as described in the text. Magnitudes of the angular spectra for  $\ell=1, 5$ , and  $10$  are shown for (b)  $G=0$ , (c)  $G=10$ , and (d)  $G=40$ .

with the phase term  $\exp(-ikr^2/2d)$  included in the latter to account for focusing.

Due to the size of the parameter space for focused sources, the results are summarized in Fig. 5 as a color-coded decision matrix in which green indicates good agreement, blue indicates borderline agreement, and purple indicates poor agreement in the vicinity of the vortex ring, with the left column corresponding to a Gaussian source, and right column to a uniform source. The subjective determination of good versus poor agreement coincides nominally with the comparisons above and below the diagonals, respectively, in Figs. 2 and 3. The parameter space covered by Fig. 5 ( $10 \leq ka \leq 200$ ,  $1 \leq \ell \leq 10$ , and  $2 \leq d/a \leq 5$ ), with emphasis on the focal region ( $z/d \sim 1$ ), coincides with experiments and applications reported in the literature.<sup>7,8,22,26,29,56–62</sup>

The largest discrepancies between results for focused Gaussian and uniform sources occur for  $d/a = 2$  (first row in Fig. 5), indicating that for the Gaussian source the accuracy of the paraxial approximation is poor for all considered values of  $ka$  and  $\ell$  due to the strong convergence of the field. In this case, the aperture half-angle  $\arctan(a/d)$  is approximately  $26^\circ$ , which is usually considered as a nominal limit on the accuracy of the paraxial approximation in the far field of an unfocused source. In the focal region of the focused Gaussian source, significant contributions to the field arrive from angles greater than  $26^\circ$  with respect to the  $z$  axis due to the spatial extent of the source beyond  $r=a$ , whereas for the uniform circular source the contributions are confined to angles less than approximately  $26^\circ$ . Solutions based on the paraxial approximation are reasonably accurate for the uniform source along the diagonal indicated by the green cells corresponding to increase in both  $ka$  and  $\ell$ .

For  $d/a = 3$  (second row in Fig. 5), there exists a range of  $ka$  and  $\ell$  for which the paraxial approximation for the Gaussian source is accurate due to reduction of the aperture half-angle to approximately  $18^\circ$ , and the paraxial approximation for the uniform source is observed to be accurate for a wider range of  $ka$  and  $\ell$  than is the case for  $d/a = 2$ . The same trend continues for  $d/a = 4$  (third row) and  $d/a = 5$  (fourth row), for which the paraxial approximation is accurate for wider ranges of  $ka$  and  $\ell$ .

Finally, of interest in a focused vortex beam is not only movement of the global maximum out of the focal plane as  $\ell$  increases, which was noted at the end of Sec. III, but also the corresponding spatial redistribution of the local maxima in the field. These phenomena are illustrated by the field plots in Fig. 6 calculated using Eq. (14) for  $G = 10$  (upper row) and  $G = 20$  (lower row). In each case, the vortex ring for  $\ell = 1$ , which is located in the plane  $z/d \simeq 1$ , is redistributed along a spheroidal surface that encloses the prefocal region as  $\ell$  increases, with the coordinates of the spheroidal surface obtained from ray theory provided in Eq. (58). Since  $G = 10$  corresponds to values of  $(ka, d/a)$  equal to either (80, 4) or (100, 5), and  $G = 20$  corresponds to either (160, 4) or (200, 5), the third and fourth rows of Fig. 5 indicate that the fields represented in Fig. 6 obtained with a solution based on

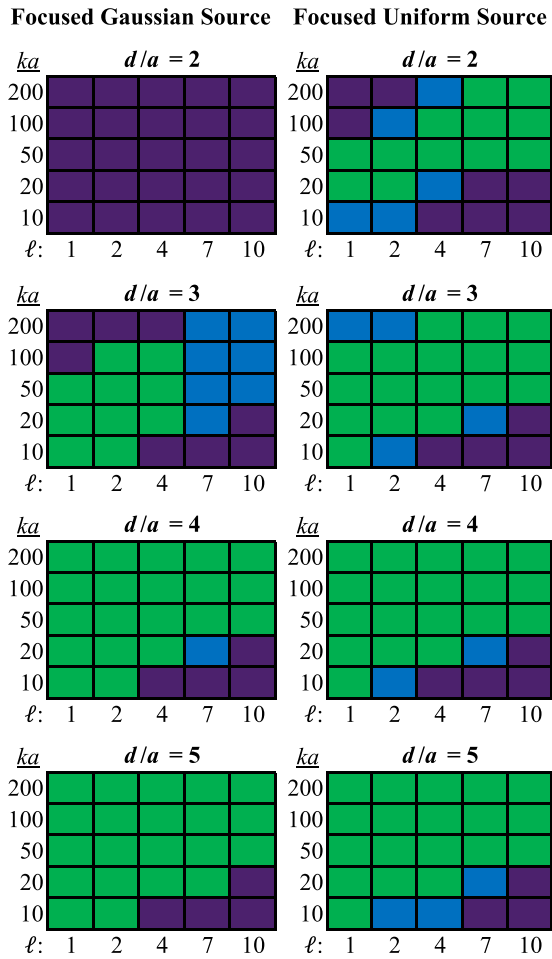


FIG. 5. (Color online) Color-coded decision matrix comparing solutions of the Helmholtz equation with solutions of its paraxial approximation for a focused Gaussian source (left column) and a focused uniform source (right column). Green indicates good agreement, blue indicates borderline agreement, and purple indicates poor agreement in the region occupied by the vortex ring near the focal plane ( $z/d \sim 1$ ). The parameter space ( $10 \leq ka \leq 200$ ,  $1 \leq \ell \leq 10$ , and  $2 \leq d/a \leq 5$ ) coincides with experiments and applications reported in the literature (Refs. 7, 8, 22, 26, 29, and 56–62).

the paraxial approximation are in good agreement with solutions of the Helmholtz equation for practical parameter values.

## VI. RAY THEORY

Insight into movement of the vortex ring out of the focal plane and toward the source as  $\ell$  increases is provided by ray theory.<sup>63</sup> In the immediate vicinity of the source plane, the pressure field  $p = qe^{ikz}$  may be expressed as

$$p(r, \theta, z) \simeq p_0 f(r) e^{i\phi}, \quad z \simeq 0, \quad (36)$$

where  $f(r)$  is the amplitude distribution in the source plane, assumed axisymmetric, and the phase

$$\phi(r, \theta, z) = -kr^2/2d + \ell\theta + kz \quad (37)$$

defines a wavefront in a focused vortex beam leaving the source plane in the paraxial approximation. For the

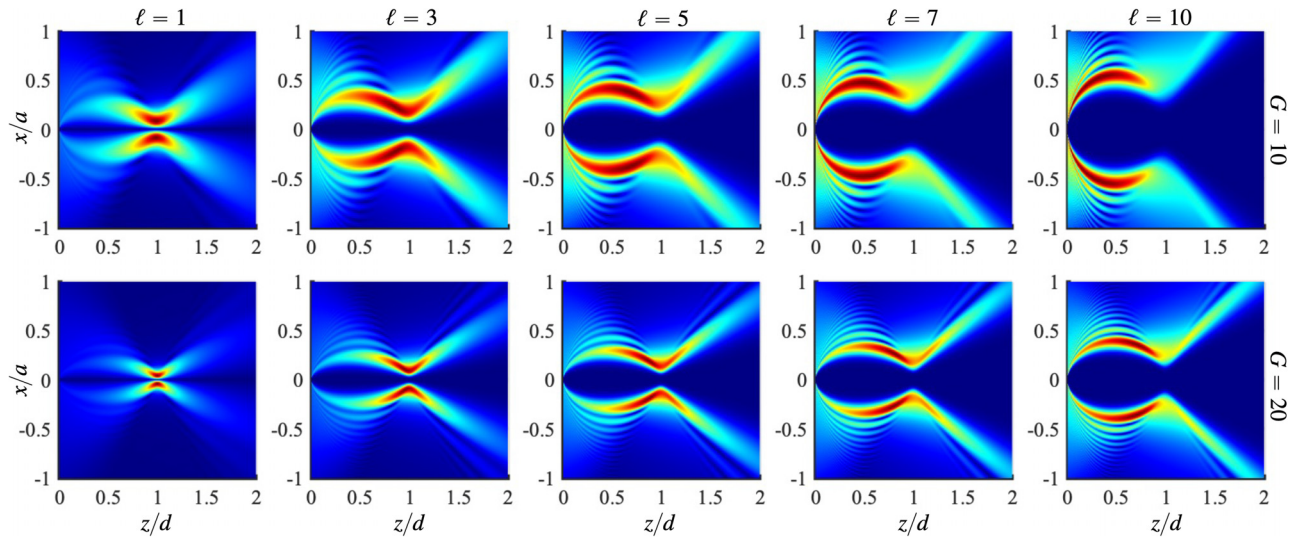


FIG. 6. (Color online) Plots of field amplitudes obtained from Eq. (14) for focused beams with  $G = 10$  (upper row) and  $G = 20$  (lower row) illustrating movement of the global maximum toward the source, and the corresponding spatial redistribution of local maxima, as  $\ell$  is increased. The color maps range from dark blue for zero pressure amplitude to dark red for maximum pressure amplitude, with the maximum amplitude specific to each combination of parameters  $G$  and  $\ell$  in order to best depict the dynamic range of the corresponding field structure.

Gaussian source condition in Eq. (4), the amplitude distribution is  $f(r) = e^{-r^2/a^2}$ . The wave normal at any point on the wavefront is defined by  $\mathbf{n} = \nabla\phi/|\nabla\phi|$ , which is evaluated for a point  $P$  in the source plane at distance  $r_0$  from the  $z$  axis to obtain

$$\mathbf{n} = \gamma^{-1}[-(r_0/d)\mathbf{e}_r + (\ell/kr_0)\mathbf{e}_\theta + \mathbf{e}_z], \quad (38)$$

where  $\gamma = [(r_0/d)^2 + (\ell/kr_0)^2 + 1]^{1/2}$  and  $|\mathbf{n}| = 1$ .

Because the medium is homogeneous, any ray emanating from the source plane follows a straight line in direction  $\mathbf{n}$ . Therefore, a ray starting at point  $P$  and traveling distance  $s$  arrives at a point  $Q$  whose position is given by the vector  $\mathbf{R} = s\mathbf{n}$  relative to point  $P$ . This relation applies to a ray emanating from any point on a circle of radius  $r_0$  in the plane  $z=0$  because  $\mathbf{R}$  is the location relative to that point on the circle. Here, and below, the word “circle” designates its perimeter and not the region enclosed by the perimeter. The family of rays emanating from the circle forms an axisymmetric surface surrounding the  $z$  axis. Thus, in any plane perpendicular to the  $z$  axis, the locations where the rays pass through that plane form a circle. The first objective is to determine the radius  $\Delta(r_0, z)$  of that circle as a function of distance  $z$  from the source plane.

The distance  $s$  along any ray path emanating from the circle of radius  $r_0$  in the plane  $z=0$  is related to the coordinate  $z$  by  $z = \mathbf{R} \cdot \mathbf{e}_z = \gamma^{-1}s$ . Therefore  $\mathbf{R} = \gamma z\mathbf{n}$ , and from Eq. (38),

$$\mathbf{R} = -(r_0 z/d)\mathbf{e}_r + (\ell z/kr_0)\mathbf{e}_\theta + z\mathbf{e}_z. \quad (39)$$

The  $r$  and  $\theta$  components form the vector  $\mathbf{r}_Q = -(r_0 z/d)\mathbf{e}_r + (\ell z/kr_0)\mathbf{e}_\theta$  for the location of point  $Q$  in the plane perpendicular to the  $z$  axis, with  $\mathbf{r}_Q$  expressed in the polar coordinate system  $(r, \theta)$  whose origin and orientation are defined by the location of point  $P$  on the circle of radius  $r_0$  in the

source plane. Since the location of the global origin  $O$  associated with the beam axis in this polar coordinate system is  $\mathbf{r}_O = -r_0\mathbf{e}_r$ , the distance between points  $Q$  and  $O$  in a plane perpendicular to the  $z$  axis is  $\Delta = |\mathbf{r}_Q - \mathbf{r}_O|$ , or

$$\frac{\Delta(r_0, z)}{r_0} = \left[ (1 - z/d)^2 + (\ell d/kr_0^2)^2 (z/d)^2 \right]^{1/2}. \quad (40)$$

More generally,  $\Delta$  is the radius of the circle formed by the family of rays emanating from the circle of radius  $r_0$  centered at the origin  $O$  in the source plane and intersecting a plane perpendicular to the  $z$  axis at an arbitrary distance from the source plane. As required, Eq. (40) reduces to  $\Delta = r_0$  at  $z = 0$ .

The vortex rings discussed in Secs. III–V are formed by radiation from the entire source plane, not from just a circle of radius  $r_0$ . Before taking into account radiation from the entire source plane, it is useful to examine first the properties of Eq. (40) for a fixed value of  $r_0$ . The vertex where  $\Delta$  is minimized is located at the value of  $z$  found by setting  $\partial\Delta/\partial z = 0$  to obtain

$$\frac{z_{\text{ver}}(r_0)}{d} = \frac{1}{1 + (\ell d/kr_0^2)^2}, \quad (41)$$

and the corresponding minimum value of  $\Delta$  is obtained by setting  $z = z_{\text{ver}}$  in Eq. (40):

$$\frac{\Delta_{\min}(r_0)}{r_0} = \frac{\ell d/kr_0^2}{\sqrt{1 + (\ell d/kr_0^2)^2}}. \quad (42)$$

Equation (40) is symmetric about  $z = z_{\text{ver}}$  in the region  $0 \leq z \leq 2z_{\text{ver}}$ . Equations (40)–(42) all depend on the dimensionless combination  $\ell d/kr_0^2$ .

Shown in Fig. 7 are plots of  $\Delta/r_0$  versus  $z/d$  obtained from Eq. (40) for  $d/kr_0^2 = 0.1$  and  $0 \leq \ell \leq 5$ . The vertex

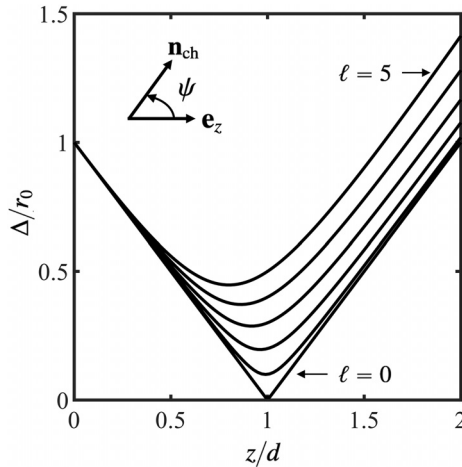


FIG. 7. Plots of  $\Delta/r_0$  versus  $z/d$  obtained from Eq. (40) for  $d/kr_0^2 = 0.1$  and  $0 \leq \ell \leq 5$  displayed with  $\ell$  increasing from bottom to top. The unit vector  $\mathbf{n}_{\text{ch}}$  and angle  $\psi$  correspond to Eq. (45), with the positive value of  $\psi$  chosen for illustration associated with the nominal directions of the annular channels following the curves in the region  $z/d \geq 1.5$ .

moves toward the source as  $\ell$  is increased according to Eq. (41), which is consistent with the direction of the shift in the location of the vortex ring observed in Fig. 6. The distance between the vertex and the  $z$  axis is observed to increase linearly with  $\ell$  as long as  $(\ell d/kr_0^2)^2$  remains small in the denominator of Eq. (42). This linear increase is consistent with the dependence of the vortex ring radius on  $\ell$  predicted by Eqs. (22) and (24).

Limiting forms of Eq. (40) are now compared with the results obtained in Sec. III. The radius of the circle in the focal plane predicted by the ray theory is, with  $z=d$  in Eq. (40),  $\Delta = \ell d/kr_0$ , which is observed to be similar to the expression for the ring radius given by Eq. (22). The result  $\Delta = \ell d/kr_0$  differs from Eq. (42) because the latter does not correspond to the radius of the circle in the focal plane, but at the location  $z_{\text{ver}}$  of the vertex predicted by ray theory, which is less than  $d$ . For an unfocused beam, evaluating Eq. (40) with  $d=\infty$  yields  $\Delta = r_0[1 + (\ell z/kr_0^2)^2]^{1/2}$ , and then evaluating this limit in the far field ( $\ell z \gg kr_0^2$ ) yields  $\Delta = \ell z/kr_0$ , which is similar to Eq. (23). Considered next is the field structure predicted by ray theory for the more general case in which radiation from the entire source plane is taken into account, not from just source points confined to a circle.

Equation (40) is now used to determine the pressure amplitude in a plane at distance  $z$  from a source possessing the arbitrary axisymmetric amplitude distribution  $p_0 f(r)$  in Eq. (36). The following relation from ray theory for the pressure amplitude  $P$  is used for this purpose,<sup>63</sup>

$$P(\Delta, z) = p_0 f(r_0) \sqrt{\frac{A(r_0, 0)}{A(r_0, z)}}, \quad (43)$$

where  $A(r_0, z)$  is the area of the annular channel corresponding to rays emanating from source points with amplitude  $p_0 f(r_0)$  at distance  $r_0$  from the  $z$  axis. The pressure  $P(\Delta, z)$  is expressed as a function of  $\Delta$  rather than  $r_0$  because the

coordinates  $(\Delta, z)$  identify the location in the field where the pressure is desired. Source point locations identified by  $r=r_0$  on the right-hand side of Eq. (43) map onto field points at  $r=\Delta(r_0, z)$  according to Eq. (40), the inversion of which permits  $r_0$  to be expressed in terms of  $(\Delta, z)$ :

$$r_0(\Delta, z) = \left[ \frac{\Delta^2 + \sqrt{\Delta^4 - \Delta_c^4(z)}}{2(1-z/d)^2} \right]^{1/2}, \quad \Delta > \Delta_c(z), \quad (44)$$

where  $\Delta_c(z)$  is defined in Eqs. (55) and (56). Regions in which  $\Delta < \Delta_c(z)$  are shadow zones ( $P=0$ ) predicted by ray theory, and Eq. (44) is not relevant in regions where there are no ray paths. Equation (44) can thus be used to evaluate the pressure amplitude in Eq. (43) as an explicit function of the field points  $(r, z) = (\Delta, z)$ . The only restriction is that the source must possess an axisymmetric amplitude distribution as described by  $p_0 f(r)$  in Eq. (36), such that the amplitude of the field throughout the vortex beam is independent of  $\theta$ , as is usually the case.

The area function  $A(r_0, z)$  in Eq. (43) usually corresponds to the cross section of a ray tube encircling a particular ray path, e.g., emanating from a point  $(r_0, \theta)$  in the source plane as defined by Eq. (38). However, of interest here is the amplitude and not the phase of the pressure, and due to the axisymmetric geometry of the annular channel formed by the family of rays radiated by a thin annulus of inner radius  $r_0$  in the source plane, the amplitude does not depend on  $\theta$ . It is therefore expedient to define  $A$  instead to be the cross-sectional area of the channel with unit normal in the  $r$ - $z$  plane forming angle  $\psi(r_0, z)$  with the  $z$  axis as defined in Fig. 7:

$$\mathbf{n}_{\text{ch}} = \sin \psi(r_0, z) \mathbf{e}_r + \cos \psi(r_0, z) \mathbf{e}_z. \quad (45)$$

The direction of the channel normal  $\mathbf{n}_{\text{ch}}$  is thus everywhere tangent to the corresponding curves in Fig. 7.

The angle  $\psi(r_0, z)$  may be expressed as  $\tan \psi = \partial \Delta / \partial z$ , which yields for the vector components in Eq. (45)

$$\sin \psi(r_0, z) = \frac{\partial \Delta / \partial z}{\sqrt{(\partial \Delta / \partial z)^2 + 1}}, \quad (46)$$

$$\cos \psi(r_0, z) = \frac{1}{\sqrt{(\partial \Delta / \partial z)^2 + 1}}, \quad (47)$$

and thus

$$\mathbf{n}_{\text{ch}} = \frac{(\partial \Delta / \partial z) \mathbf{e}_r + \mathbf{e}_z}{\sqrt{(\partial \Delta / \partial z)^2 + 1}}, \quad (48)$$

where

$$\frac{\partial \Delta}{\partial z} = -\frac{r_0}{d} \frac{1 - z/d - (\ell d/kr_0^2)^2 z/d}{\left[ (1 - z/d)^2 + (\ell d/kr_0^2)^2 (z/d)^2 \right]^{1/2}}. \quad (49)$$

The form of Eq. (48) facilitates comparison with the wave normal  $\mathbf{n}$  defined by Eq. (38), which determines the directions of the ray paths within the annular channel.

Only for  $\ell=0$  is  $\mathbf{n}_{\text{ch}}$  equivalent to  $\mathbf{n}$ :

$$\mathbf{n}_{\text{ch}} = \frac{-\text{sgn}(1-z/d)(r_0/d)\mathbf{e}_r + \mathbf{e}_z}{\sqrt{(r_0/d)^2 + 1}}, \quad \ell = 0. \quad (50)$$

In this case, the component  $\mathbf{e}_\theta$  in Eq. (38) vanishes, and all rays intersect the  $z$  axis at  $z=d$ . Equation (50) describes a conical structure for the annular channel that is symmetric about its vertex in the plane  $z=d$  as illustrated in Fig. 7, and in the first column of Fig. 8 below. Since the expression for  $\mathbf{n}$  in Eq. (38) is restricted to the source plane, unlike Eq. (50) it does not account for the sign change in the coefficient of  $\mathbf{e}_r$  beyond the focal plane  $z=d$ , where the ray paths diverge from the  $z$  axis.

For  $\ell \neq 0$ , the nonzero component  $\mathbf{e}_\theta$  in Eq. (38) prevents  $\mathbf{n}_{\text{ch}}$  from being equivalent to  $\mathbf{n}$ . Although  $\mathbf{n}_{\text{ch}}$  can be the projection of  $\mathbf{n}$  onto the  $r$ - $z$  plane, this occurs only for two values of  $z$ :

$$\mathbf{n}_{\text{ch}} = \frac{-\text{sgn}(1-z/z_{\text{ver}})(r_0/d)\mathbf{e}_r + \mathbf{e}_z}{\sqrt{(r_0/d)^2 + 1}}, \quad \ell \neq 0, \quad z = 0 \text{ or } 2z_{\text{ver}}, \quad (51)$$

where  $z_{\text{ver}}$  is the location of the minimum channel radius, as defined in Eq. (41). Equation (51) applies only in the plane  $z=0$  or  $z=2z_{\text{ver}}$ , and nowhere else. Apart from the sign change for  $z=2z_{\text{ver}}$  associated with divergence of the rays in the region  $z>z_{\text{ver}}$ , Eq. (51) is observed to be equivalent to Eq. (38) if the component  $\mathbf{e}_\theta$  is removed. More generally, as noted following Eq. (42), the annular channel radius  $\Delta(r_0, z)$  is symmetric about the vertex at  $z=z_{\text{ver}}$  in the region  $0 \leq z \leq 2z_{\text{ver}}$ ; therefore,  $\psi$  is symmetric about this turning point, with  $\psi < 0$  for  $z < z_{\text{ver}}$ ,  $\psi = 0$  at  $z = z_{\text{ver}}$ , and  $\psi > 0$  for  $z > z_{\text{ver}}$ .

It also proves convenient to express the cross-sectional area  $A$ , the orientation of which is defined by Eqs. (45) and (48), in terms of the cross-sectional area  $A_z$  formed by the intersection of the annular ray channel with any plane perpendicular to the  $z$  axis, such that  $A_z$  has unit normal  $\mathbf{e}_z$ :

$$A(r_0, z) = A_z(r_0, z) \cos \psi(r_0, z). \quad (52)$$

In Eq. (43),  $p_0 f(r_0)$  is thus the pressure amplitude in a thin annulus of inner radius  $r_0$  and area  $A_z(r_0, 0)$  in the source plane  $z=0$ , and  $P(\Delta, z)$  is the pressure amplitude in the corresponding annular ray channel of inner radius  $\Delta(r_0, z)$  and area  $A_z(r_0, z)$  at  $z \geq 0$ . The annulus of inner radius  $r_0$  at  $z=0$  is assigned an infinitesimal width  $w$  such that its area is  $A_z(r_0, 0) = 2\pi r_0 w$ , with the area of the annular channel at distances  $z \geq 0$  given by

$$\begin{aligned} A_z(r_0, z) &= 2\pi\Delta(r_0, z)|\Delta(r_0 + w, z) - \Delta(r_0, z)| \\ &\simeq 2\pi\Delta(r_0, z)w|\partial\Delta/\partial r_0| \\ &= 2\pi r_0 w|(1-z/d)^2 - (\ell d/k r_0^2)^2(z/d)^2|. \end{aligned} \quad (53)$$

Combining Eqs. (43), (52), and (53) yields

$$P(\Delta, z) = p_0 f(r_0) \left[ \frac{\cos \psi(r_0, 0) / \cos \psi(r_0, z)}{|(1-z/d)^2 - (\ell d/k r_0^2)^2(z/d)^2|} \right]^{1/2} \quad (54)$$

for the pressure amplitude in the annulus of inner radius  $r=\Delta(r_0, z)$  at distances  $z \geq 0$  from the source plane and  $r > \Delta_c(z)$  from the  $z$  axis due to the family of rays emanating from the annulus of inner radius  $r=r_0$  in the source plane.

Of interest in the present section are the shift and distortion of the vortex ring depicted in Fig. 6 as  $\ell$  increases. These spatial features are associated with the caustics created by the vorticity of the sound field. Caustics are paths along which cross-sectional areas of the annular ray channels vanish and the corresponding pressure amplitude predicted by ray theory is infinite. Setting  $A_z(r_0, z) = 0$  in Eq. (53), which results in an equation that is quadratic in  $z$ , yields the two roots  $z/d = (1 \pm \ell d/k r_0^2)^{-1}$ . The roots are rewritten as  $r_0^2 = \pm(\ell z/k)/(1-z/d)$  and substituted into Eq. (40) to obtain the path of the caustic:

$$\Delta_c(z) = \sqrt{(2\ell d/k)(z/d)|1-z/d|}. \quad (55)$$

For comparison with Eq. (14), and to facilitate interpretation,  $\Delta_c(z)$  is normalized by the characteristic source radius  $a$ :

$$\frac{\Delta_c(z)}{a} = \sqrt{(\ell/G)(z/d)|1-z/d|}, \quad (56)$$

where  $G = ka^2/2d$  as before. It is observed that  $\Delta_c(z)$  is zero at  $z=0$  and  $z=d$ , and in between it is symmetric about  $z=\frac{1}{2}d$ , at which point the caustic in the region  $z < d$  is furthest from the  $z$  axis, with the distance from the  $z$  axis given by  $\Delta_c/a = \frac{1}{2}\sqrt{\ell/G}$ . For  $z \gg d$ , the distance between the caustic and the  $z$  axis increases linearly with  $z$  according to  $\Delta_c/a \simeq \sqrt{\ell/G}(z/d)$ . The normalized form of Eq. (40) for the path of each annular ray channel in the  $r$ - $z$  plane is given by

$$\frac{\Delta(r_0, z)}{a} = \frac{r_0}{a} \left[ (1-z/d)^2 + \frac{(\ell/2G)^2(z/d)^2}{(r_0/a)^4} \right]^{1/2}, \quad (57)$$

with the coordinates for where the distance between each path and the  $z$  axis is minimized given by Eqs. (41) and (42). For  $\ell=0$  the result for the caustic reduces to  $\Delta_c(z)=0$ , merely indicating that the caustic vanishes, and Eq. (57) reduces to the result for a converging spherical wave,  $\Delta(r_0, z) = r_0|1-z/d|$ .

Shown in Fig. 8 are overlays of Eq. (56) for the caustics (thick white curves) and Eq. (57) for the annular ray channels (thin white curves) on top of color plots for the amplitude of the pressure field obtained from Eq. (14) for  $G=10$  (first row) and  $G=20$  (second and third rows), with  $\ell=0, 1, 2, 3, 4$ , and 5 for the six columns in the first and second row,

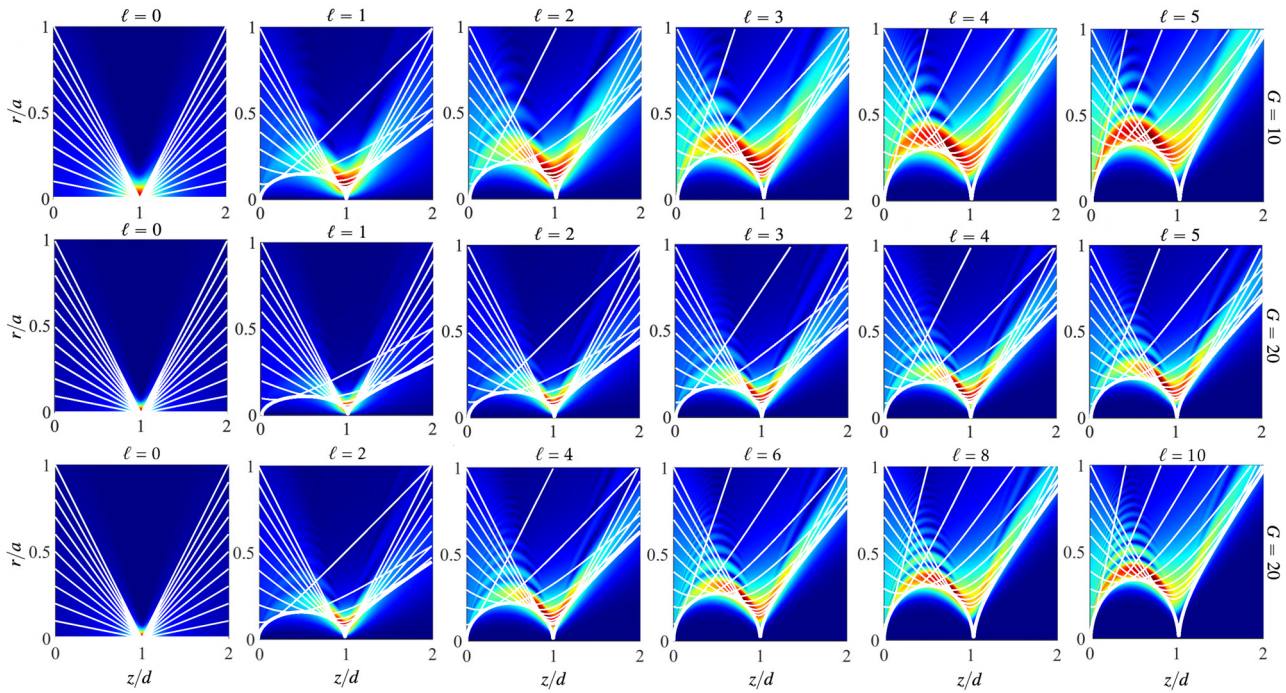


FIG. 8. (Color online) Overlays of Eq. (56) for the caustics (thick white curves) and Eq. (57) for the annular ray channels (thin white curves) on top of color plots for the amplitude of the pressure field obtained from Eq. (14) for  $G = 10$  (first row) and  $G = 20$  (second and third rows) illustrating movement of the global maximum toward the source, and the corresponding spatial redistribution of local maxima, as  $\ell$  is increased in the range  $0 \leq \ell \leq 5$  in the first and second rows and  $0 \leq \ell \leq 10$  in the third row. For clarity, only annular ray channels emanating from the region  $0 \leq r/a \leq 1$  in the source plane are displayed. See caption of Fig. 5 for explanation of the color maps.

and  $\ell = 0, 2, 4, 6, 8$ , and  $10$  in the third row (i.e., double the corresponding values in the first two rows). The parameters match those in Fig. 6 in order to illustrate how, as  $\ell$  is increased, ray theory can be used to interpret the movement of the global maximum toward the source and the corresponding spatial redistribution of local maxima. Figures 6 and 8 are somewhat different in appearance because in the latter only the upper half of the field is displayed, and with the vertical axes expanded in order to better resolve the features of the annular ray channels. For clarity, only channels emanating from the region  $0 \leq r/a \leq 1$  in the source plane are displayed. One consequence of this truncation is that channels forming the bottom of the “V” in the caustic at  $z/d = 1$  are absent, e.g., especially for  $G = 10$  and  $\ell = 5$ .

It is observed in Fig. 8 that Eq. (56) for the caustic defines rather well the shadow zones in both the prefocal and postfocal regions. It is also observed that the trajectory of the global maximum follows the caustic in the direction of the source as  $\ell$  increases. Comparing the first and second rows as  $\ell$  is increased from 0 to 5 reveals that the movement of the global maximum toward the source is less pronounced for  $G = 20$  (second row) than for  $G = 10$  (first row). However, comparing the first and third rows as  $\ell$  is increased from 0 to 5 in the former ( $G = 10$ ) but from 0 to 10 in the latter ( $G = 20$ ), it is observed that the movement of the global maximum toward the source is very much the same even though the values of  $G$  differ by a factor of 2. This is due to the fact that the paths of the annular ray channels defined by Eq. (40), and the paths of the caustics defined by Eq. (55), do not vary with  $\ell$  and  $k$  when the ratio

$\ell/k$  is held constant, which corresponds to maintaining a constant ratio  $\ell/G$  in Eqs. (56) and (57). The main difference in the field calculations based on Eq. (14) in the first and third rows is the higher spatial frequency in the third row, which corresponds to the value of  $k$  being doubled. Starting with Eq. (38), all subsequent equations in the present section depend on  $\ell$  and  $k$  only in the ratio  $\ell/k$ , including the equations in the last paragraph for unfocused vortex beams.

We now examine the geometry of the shadow zone in the prefocal region. Letting  $(x_c, y_c, z_c)$  be the coordinates of the surface defined by the caustic, one may write  $\Delta_c^2 = x_c^2 + y_c^2$  and rearrange Eq. (56) to obtain

$$\frac{x_c^2 + y_c^2}{a_c^2} + \frac{(z_c - d/2)^2}{c_c^2} = 1, \quad 0 \leq z_c \leq d, \quad (58)$$

which describes a spheroid in the prefocal region centered at  $z_c = d/2$  along its axis of symmetry with

$$a_c^2 = \ell a^2 / 4G, \quad c_c^2 = d^2 / 4. \quad (59)$$

Equation (58) corresponds to a prolate spheroid for  $a_c < c_c$  and an oblate spheroid for  $a_c > c_c$ , or

$$(d/a)^2 G > \ell, \quad \text{prolate spheroid}, \quad (60)$$

$$(d/a)^2 G < \ell, \quad \text{oblate spheroid}. \quad (61)$$

One may also write  $(d/a)^2 G = \pi d/\lambda$ , where  $\lambda = 2\pi/k$ , and therefore whether the shape of the shadow zone predicted by ray theory in the prefocal region is prolate or oblate

depends only on the ratio of focal length to wavelength relative to the orbital number. Since the volume of the spheroid is  $\frac{4}{3}\pi a_c^2 c_c$ , the volume of the shadow zone enclosed by the caustic surface in the prefocal region may be expressed as  $V_c = \frac{1}{6}\ell\lambda d^2$ , in which the product  $\ell\lambda$  is a consequence of the ratio  $\ell/k$  that is discussed in connection with Fig. 8.

Figure 5 indicates that the paraxial approximation is accurate in the parameter space defined by  $d/a \geq 4$ ,  $ka \geq 50$ , and  $1 \leq \ell \leq 10$ , in which case for  $G \geq 5$  one obtains  $(d/a)^2 G \geq 80$ . Thus, the caustic surface in the prefocal region is a prolate spheroid for all cases considered in Figs. 6 and 8. The prefocal caustic surface for  $G = 10$  and  $\ell = 5$  in Fig. 8 (and for  $G = 20$  and  $\ell = 10$  as well) appears oblate rather than prolate only because of the aspect ratio employed to emphasize the field structure surrounding the caustic. Oblate spheroids may be encountered under other circumstances.

Prefocal shadow zones like those in Fig. 6 are not restricted to vortex beams with Gaussian amplitude shading. For example, a source amplitude described by a raised cosine of finite extent defined by  $f(r) = \frac{1}{2}[1 + \cos(\pi r/2a)]$  for  $0 \leq r \leq a$  and zero otherwise in place of  $f(r) = e^{-r^2/a^2}$  in Eq. (4) produces field patterns very similar to those in Fig. 6. The spheroidal cavities surrounded by steep pressure gradients in Fig. 6 may prove useful for particle trapping in three dimensions, a subject of interest in recent studies.<sup>26,64</sup>

A wave phenomenon referred to in optics as an autofocusing vortex beam<sup>47</sup> bears resemblance to the field structures in the regions corresponding to  $z > d/2$  in Fig. 8. The autofocusing effect is created by positioning the source plane at  $z > d/2$ . Instead of the phase term  $-kr^2/d$  at  $z = 0$  in Eq. (37), a different phase term is used at  $z > d/2$  to produce an abruptly converging vortex field in the region  $z > d/2$  that follows a caustic similar to Eq. (55). In addition to the significantly different source conditions used to create the autofocusing effect, the expressions for the caustics do not lend themselves to describing the field produced by the source condition in Eqs. (36) and (37) and exhibited throughout the regions  $z > 0$  in Fig. 8. A number of other publications on autofocusing optical beams, dating back to 2010, are reported by Xiao *et al.*<sup>47</sup>

Finally, simplified forms of the results obtained with ray theory for focused vortex beams are considered in the absence of focusing. With  $d = \infty$ , Eqs. (40) and (53) for the distance between the annular ray channel and the  $z$  axis, and the corresponding cross-sectional area of the channel perpendicular to the  $z$  axis, reduce to

$$\Delta(r_0, z) = r_0 \left[ 1 + (\ell z / kr_0^2)^2 \right]^{1/2} \quad (62)$$

and

$$A_z(r_0, z) = 2\pi r_0 w |1 - (\ell z / kr_0^2)^2|, \quad (63)$$

respectively. The limiting forms of Eqs. (41) and (42),  $z_{\text{ver}} = 0$  and  $\Delta_{\min} = r_0$ , merely reflect the fact that  $\Delta$  increases continuously with distance from the source plane

for  $\ell > 0$ , and it remains constant for  $\ell = 0$ . Equation (55) for the caustic becomes

$$\Delta_c(z) = \sqrt{2\ell z / k}, \quad (64)$$

which for  $\ell > 0$  defines a paraboloid that increases in proportion to  $z^{1/2}$  from the source plane to the far field. The amplitude of the pressure field outside the shadow zone enclosed by the paraboloidal caustic surface is, from Eq. (54),

$$P(\Delta, z) = p_0 f(r_0) \left[ \frac{\cos \psi(r_0, 0) / \cos \psi(r_0, z)}{|1 - (\ell z / kr_0^2)^2|} \right]^{1/2}, \quad (65)$$

and Eq. (44), which is used to express  $r_0$  as a function of  $(\Delta, z)$ , reduces to

$$r_0(\Delta, z) = 2^{-1/2} \left[ \Delta^2 + \sqrt{\Delta^4 - \Delta_c^4(z)} \right]^{1/2}, \quad \Delta > \Delta_c(z). \quad (66)$$

Equations (46) and (47) defining the angle  $\psi$  of the annular ray channel in the  $r-z$  plane retain the same forms, but Eq. (49) reduces to

$$\frac{\partial \Delta}{\partial z} = \frac{\ell}{kr_0} \frac{\ell z / kr_0^2}{\sqrt{1 + (\ell z / kr_0^2)^2}}, \quad (67)$$

which for  $\ell > 0$  further reduces to  $\ell / kr_0$  in the far field ( $\ell z \gg kr_0^2$ ). For  $\ell = 0$  one obtains  $\psi = 0$ , and all ray channels

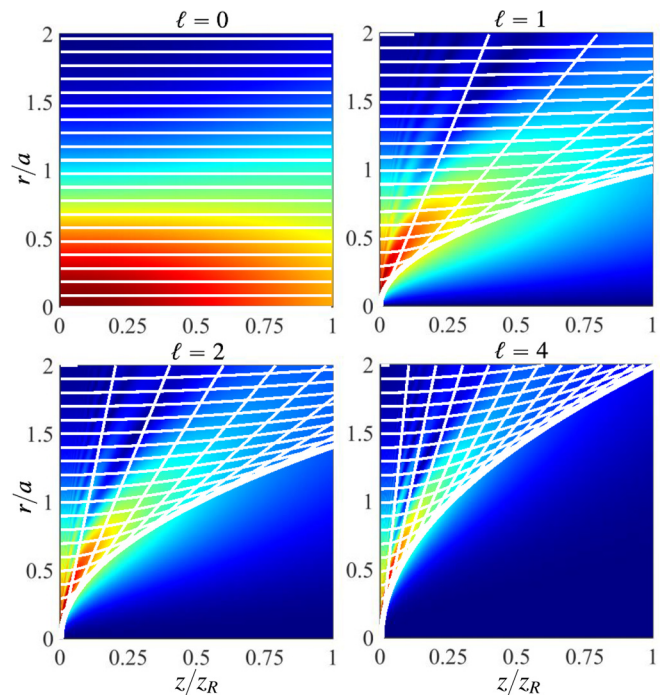


FIG. 9. (Color online) Overlays of Eq. (64) for the caustics (thick white curves) and Eq. (62) for the annular ray channels (thin white curves) on top of color plots for the amplitude of the pressure field obtained from Eq. (14) for  $d = \infty$  (no focusing) and several values of  $\ell$ . In terms of the Rayleigh distance  $z_R = ka^2/2$  appearing in the figure, Eq. (64) may be expressed as  $\Delta/a = (\ell z / z_R)^{1/2}$ . See caption of Fig. 6 for explanation of the color maps.

are parallel to the  $z$  axis. In Fig. 9, Eqs. (62) and (64) are overlayed on the amplitude of the pressure field obtained from Eq. (14) for several values of  $\ell$ .

## VII. SUMMARY

Focused acoustic vortex beams have been studied extensively for use as acoustic tweezers that exploit the pressure minimum along the axis to trap particles, and unfocused vortex beams are being considered for high-speed communication that employs multiplexing based on the orbital number. Mathematical models for both applications are frequently based on the paraxial approximation to simplify the analysis, which is also used extensively in optics. The paraxial approximation can be particularly useful when taking into account nonlinear propagation effects in an acoustic vortex beam.<sup>65</sup>

One purpose of the present work was to assess the accuracy of the paraxial approximation when applied to vortex beams. This was facilitated by using a compact analytical expression based on the paraxial approximation for a vortex beam radiated by a source with a Gaussian amplitude distribution, with or without focusing. Comparisons with solutions of the Helmholtz equation demonstrated that, for the paraxial approximation of an unfocused beam to be accurate, the value of  $ka$  for the source should be several times larger than the value of the orbital number up to at least  $\ell = 10$ . Focusing introduces the ratio  $d/a$  of focal length to source radius, and it also significantly alters the structure of the angular spectra, the combination of which prevented determination of a simple analytical criterion for agreement with the Helmholtz equation. Values of  $d/a$ ,  $ka$ , and  $\ell$  for which the paraxial approximation of a focused vortex beam is reasonably accurate were presented using the decision matrix in Fig. 5.

It was found that as  $\ell$  increases for a focused vortex beam, the vortex ring moves out of the focal plane in the direction of the source, and for  $10 \leq G \leq 20$  ( $G = ka^2/2d$ ) the maximum amplitude is redistributed along a spheroidal surface enclosing a shadow zone in the prefocal region. These observations motivated development of a model based on ray theory for a source with an axisymmetric amplitude distribution. The main result obtained from ray theory is a simple expression for the coordinates of the caustic surface formed in a vortex beam, and especially the spheroidal surface formed by local amplitude maxima in the prefocal region of a focused vortex beam. Also obtained is an explicit expression based on ray theory for the pressure amplitude in a vortex beam.

The paraxial and ray approximations presented here provide simple analytical expressions and physical insights for features of acoustic vortex beams that have not previously been investigated in detail but may prove useful for applications in science and engineering.

## ACKNOWLEDGMENTS

C.A.G. was supported by the Applied Research Laboratories Chester M. McKinney Graduate Fellowship in Acoustics.

## AUTHOR DECLARATIONS

### Conflict of Interest

The authors have no conflicts to disclose.

## DATA AVAILABILITY

The data that support the findings of this study are available within the article.

## APPENDIX: LAGUERRE-GAUSS EXPANSION

Presented here for comparison with Eq. (12) is a common alternative solution for vortex beams based on an expansion in terms of Laguerre-Gaussian modes. The comparison is restricted to unfocused Gaussian sources with vorticity, Eq. (4) with  $d = \infty$ :

$$q(r, \theta, 0) = p_0 e^{-r^2/d^2} e^{i\ell\theta}, \quad d = \infty. \quad (\text{A1})$$

While the focused source condition in Eq. (4) is recovered by replacing  $a^2$  in Eq. (A1) with the complex quantity  $\tilde{a}^2 = a^2/(1 + ika^2/2d)$ , this introduces complications in the standard Laguerre-Gauss formulation that are unnecessary for the purpose of comparing the expansions with Eq. (12). Specifically, it is demonstrated below that for all  $\ell \neq 0$  an infinite number of Laguerre-Gaussian modes is required to describe the radiated field corresponding to the source condition in Eq. (A1).

The solution of Eq. (2), the paraxial approximation of the Helmholtz equation, is thus sought in terms of the expansion

$$q(r, \theta, z) = \sum_{n,m} A_n^m \text{LG}_{nm}(r, \theta, z) \quad (\text{A2})$$

with the Laguerre-Gaussian modes expressed in the standard form

$$\begin{aligned} \text{LG}_{nm}(r, \theta, z) = & \frac{N_n^m}{w(z)} \left( \frac{\sqrt{2}r}{w(z)} \right)^{|m|} L_n^{|m|} \left( \frac{2r^2}{w^2(z)} \right) \exp \left( -\frac{r^2}{w^2(z)} \right) \\ & \times \exp \left\{ i \left[ m\theta + \frac{kr^2}{2R(z)} - (2n+|m|+1)\phi(z) \right] \right\}, \end{aligned} \quad (\text{A3})$$

where  $L_n^m$  are the Laguerre polynomials. The quantities

$$\left. \begin{aligned} w(z) &= w_0 \sqrt{1 + (z/z_w)^2}, \\ R(z) &= z \left[ 1 + (z_w/z)^2 \right], \\ \phi(z) &= \arctan(z/z_w), \end{aligned} \right\} \quad (\text{A4})$$

are functions of distance relative to the diffraction length  $z_w = kw_0^2/2$  associated with the characteristic beam radius  $w_0$ , and  $N_n^m = \{2n!/\left[\pi(n+|m|)!\right]\}^{1/2}$  is a normalization factor that yields

$$\int_0^{2\pi} \int_0^{\infty} \text{LG}_{nm}(r, \theta, z) \text{LG}_{n'm'}^*(r, \theta, z) r dr d\theta = \delta_{nn'} \delta_{mm'} \quad (\text{A5})$$

for the orthogonality integral, where  $\delta_{\alpha\beta}$  is the Kronecker delta and the asterisk indicates complex conjugate.

The expansion coefficients in Eq. (A2) are obtained as follows. Evaluation of Eq. (A3) at  $z=0$  to obtain

$$\text{LG}_{nm}(r, \theta, 0) = N_n^m \frac{1}{w_0} \left( \frac{\sqrt{2}r}{w_0} \right)^{|m|} L_n^{|m|} \left( \frac{2r^2}{w_0^2} \right) e^{-r^2/w_0^2} e^{im\theta}, \quad (\text{A6})$$

and then substitution of Eqs. (A1) and (A6) into Eq. (A2) followed by multiplication of each side by  $\text{LG}_{n'm'}^*$ , integration over the plane  $z=0$  making use of the orthogonality relation in Eq. (A5), and noting that  $\int_0^{2\pi} e^{i(\ell-m')\theta} d\theta = 2\pi \delta_{\ell m'}$  yields

$$A_n^{\ell} = 2\pi N_n^{\ell} \frac{p_0}{w_0} \int_0^{\infty} \left( \frac{\sqrt{2}r}{w_0} \right)^{|\ell|} L_n^{|\ell|} \left( \frac{2r^2}{w_0^2} \right) e^{-(a^{-2}+w_0^{-2})r^2} r dr \quad (\text{A7})$$

for the coefficients in the resulting summation over the single index  $n$ :

$$q(r, \theta, z) = \sum_{n=0}^{\infty} A_n^{\ell} \text{LG}_{n\ell}(r, \theta, z). \quad (\text{A8})$$

Simplification is achieved by setting  $w_0=a$  and then letting  $x=2r^2/a^2$  to obtain

$$A_n^{\ell} = \frac{\pi}{2} N_n^{\ell} B_n^{\ell} p_0 a, \quad (\text{A9})$$

where the integral in Eq. (A7), which becomes

$$B_n^{\ell} = \int_0^{\infty} x^{|\ell|/2} L_n^{|\ell|}(x) e^{-x} dx = \frac{\Gamma(1+\ell/2)\Gamma(n+\ell/2)}{n! \Gamma(\ell/2)}, \quad (\text{A10})$$

is expressed in terms of gamma functions.<sup>50</sup> The Laguerre-Gaussian modes in Eq. (A3) are thus evaluated with  $m=\ell$ ,  $w_0=a$ , and  $z_w=z_R=ka^2/2$ , making Eq. (A8) equivalent to Eq. (12) with  $d=\infty$  in Eq. (13).

For  $\ell=0$ , Eq. (A10) yields

$$B_n^0 = \frac{\Gamma(1)\Gamma(n)}{n! \Gamma(0)} = \delta_{n0}, \quad (\text{A11})$$

and therefore  $B_0^0 = 1$ , with  $B_n^0 = 0$  for all  $n > 0$  because  $\Gamma(0) = \infty$ . The summation in Eq. (A8) thus reduces to the single term  $n=0$ ,

$$q(r, z) = A_0^0 \text{LG}_{00}(r, z), \quad \ell = 0. \quad (\text{A12})$$

Although less compact with  $\text{LG}_{00}$  expressed as in Eq. (A3), Eq. (A12) is equivalent to Eq. (17). For this degenerate case

( $\ell=0$ , no vorticity), involving only one mode in the expansion ( $n=0$ ), there is no advantage to using Eq. (12).

However, Eq. (A10) reveals that for all nonzero values of  $\ell$ ,  $B_n^{\ell}$  is nonzero for all  $n$ ; therefore, all modes in Eq. (A8) are required for  $\ell \neq 0$ . For example, with  $\ell=1$  and  $\ell=2$  one obtains

$$B_n^1 = \frac{\Gamma(3/2)\Gamma(n+1/2)}{n! \Gamma(1/2)} = \frac{\sqrt{\pi}(2n)!}{2(4^n)(n!)^2}, \quad (\text{A13})$$

$$B_n^2 = \frac{\Gamma(2)\Gamma(n+1)}{n! \Gamma(1)} = 1, \quad (\text{A14})$$

and Eq. (A8) yields

$$q(r, \theta, z) = p_0 e^{i\theta} \frac{r/a}{|\zeta(z)|^2} \exp \left( -\frac{r^2/a^2}{\zeta(z)} \right) \times \sqrt{\pi/2} \sum_{n=0}^{\infty} \frac{(2n)! e^{-i(2n+2)\phi_R(z)}}{4^n (n+1) (n!)^2} L_n^1 \left( \frac{2r^2/a^2}{|\zeta(z)|^2} \right), \quad \ell = 1, \quad (\text{A15})$$

$$q(r, \theta, z) = p_0 e^{i2\theta} \frac{r^2/a^2}{|\zeta(z)|^3} \exp \left( -\frac{r^2/a^2}{\zeta(z)} \right) \times 2 \sum_{n=0}^{\infty} \frac{e^{-i(2n+3)\phi_R(z)}}{(n+1)(n+2)} L_n^2 \left( \frac{2r^2/a^2}{|\zeta(z)|^2} \right), \quad \ell = 2, \quad (\text{A16})$$

where  $\zeta(z) = 1 + iz/z_R$ ,  $\phi_R(z) = \arctan(z/z_R)$ , and  $z_R = ka^2/2$ .

In addition to the complexity of the Laguerre-Gauss expansions for  $\ell \neq 0$  compared with Eq. (12), the number of terms required for convergence increases with  $\ell$ . For  $\ell=1$ , 2, and 3, approximately 10, 20, and 30 terms, respectively, are required for the magnitude of Eq. (A8) to achieve reasonable agreement with Eq. (14) at distances  $z/z_R \gtrsim 0.2$ . Significantly more terms are required for comparable agreement in phase.

The reader is referred to Pan *et al.*<sup>66</sup> for numerical evaluations of the Laguerre-Gauss expansion coefficients corresponding to the source condition in Eq. (A1), rather than the explicit analytical expressions presented in Eqs. (A9) and (A10).

<sup>1</sup>L. Allen, M. W. Beijersbergen, R. J. C. Spreeuw, and J. Woerdman, “Orbital angular momentum of light and the transformation of Laguerre-Gaussian laser modes,” *Phys. Rev. A* **45**, 8185–8189 (1992).

<sup>2</sup>Y. Shen, X. Wang, Z. Xie, C. Min, X. Fu, Q. Liu, M. Gong, and X. Yuan, “Optical vortices 30 years on: OAM manipulation from topological charge to multiple singularities,” *Light: Sci. Appl.* **8**, 90 (2019).

<sup>3</sup>P. Coullet, L. Gil, and F. Rocca, “Optical vortices,” *Opt. Commun.* **73**, 403–408 (1989).

<sup>4</sup>H. von Helmholtz, “On integrals of the hydrodynamical equations, which express vortex-motion,” *Philos. Mag.* **33**, 485–512 (1867).

<sup>5</sup>B. T. Hefner and P. L. Marston, “An acoustical helicoidal wave transducer with applications for the alignment of ultrasonic and underwater systems,” *J. Acoust. Soc. Am.* **106**, 3313–3316 (1999).

<sup>6</sup>L. Zhang and P. L. Marston, “Angular momentum flux of nonparaxial acoustic vortex beams and torques on axisymmetric objects,” *Phys. Rev. E* **84**, 065601 (2011).

- <sup>7</sup>A. Anhäuser, R. Wunenburger, and E. Brasselet, "Acoustic rotational manipulation using orbital angular momentum transfer," *Phys. Rev. Lett.* **109**, 034301 (2012).
- <sup>8</sup>R. Wunenburger, J. I. V. Lozano, and E. Brasselet, "Acoustic orbital angular momentum transfer to matter by chiral scattering," *New J. Phys.* **17**, 103022 (2015).
- <sup>9</sup>Z. Hong, J. Zhang, and B. W. Drinkwater, "Observation of orbital angular momentum transfer from Bessel-shaped acoustic vortices to biphasic liquid-microparticle mixtures," *Phys. Rev. Lett.* **114**, 214301 (2015).
- <sup>10</sup>T. Wang, M. Ke, W. Li, Q. Yang, C. Qiu, and Z. Liu, "Particle manipulation with acoustic vortex beam induced by a brass plate with spiral shape structure," *Appl. Phys. Lett.* **109**, 123506 (2016).
- <sup>11</sup>M. Baudoin, J.-C. Gerbedoen, A. Riaud, O. B. Matar, N. Smagin, and J.-L. Thomas, "Folding a focalized acoustical vortex on a flat holographic transducer: Miniaturized selective acoustical tweezers," *Sci. Adv.* **5**, eaav1967 (2019).
- <sup>12</sup>Z. Gong and M. Baudoin, "Particle assembly with synchronized acoustic tweezers," *Phys. Rev. Appl.* **12**, 024045 (2019).
- <sup>13</sup>A. Marzo and B. W. Drinkwater, "Holographic acoustic tweezers," *Proc. Natl. Acad. Sci. U.S.A.* **116**, 84–89 (2019).
- <sup>14</sup>T. M. Marston and P. L. Marston, "Modulated helicity for acoustic communications and helicity-selective acoustic receivers," *J. Acoust. Soc. Am.* **127**, 1856 (2010).
- <sup>15</sup>V. Bollen, D. J. Zartman, T. M. Marston, and P. L. Marston, "Measured scattering of a first-order vortex beam by a sphere: Cross-helicity and helicity-neutral near-forward scattering and helicity modulation," *Proc. Mtgs. Acoust.* **19**, 070075 (2013).
- <sup>16</sup>C. Shi, M. Dubois, Y. Wang, and X. Zhang, "High-speed acoustic communication by multiplexing orbital angular momentum," *Proc. Natl. Acad. Sci. U.S.A.* **114**, 7250–7253 (2017).
- <sup>17</sup>X. Jiang, B. Liang, J.-C. Cheng, and C.-W. Qiu, "Twisted acoustics: Metasurface-enabled multiplexing and demultiplexing," *Adv. Mater.* **30**, 1800257 (2018).
- <sup>18</sup>X. Jiang, C. Shi, Y. Wang, J. Smalley, J. Cheng, and X. Zhang, "Nonresonant metasurface for fast decoding in acoustic communications," *Phys. Rev. Appl.* **13**, 014014 (2020).
- <sup>19</sup>Z. Sun, Y. Shi, X. Sun, H. Jia, Z. Jin, K. Deng, and J. Yang, "Underwater acoustic multiplexing communication by pentamode metasurface," *J. Phys. D: Appl. Phys.* **54**, 205303 (2021).
- <sup>20</sup>M. E. Kelly and C. Shi, "Design and simulation of acoustic vortex wave arrays for long-range underwater communication," *JASA Express Lett.* **3**, 076001 (2023).
- <sup>21</sup>A. Ozcelik, J. Rufo, F. Guo, Y. Gu, P. Li, J. Lata, and T. J. Huang, "Acoustic tweezers for the life sciences," *Nat. Methods* **15**, 1021–1028 (2018).
- <sup>22</sup>S. Jiménez-Gambín, N. Jiménez, and F. Camarena, "Transcranial focusing of ultrasonic vortices by acoustic holograms," *Phys. Rev. Appl.* **14**, 054070 (2020).
- <sup>23</sup>S. Guo, Z. Ya, P. Wu, L. Zhang, and M. Wan, "Enhanced sonothrombolysis induced by high-intensity focused acoustic vortex," *Ultrasound Med. Biol.* **48**, 1907–1917 (2022).
- <sup>24</sup>N. Jiménez, J. P. Groby, and V. Romero-García, "Spiral sound-diffusing metasurfaces based on holographic vortices," *Sci. Rep.* **11**, 10217 (2021).
- <sup>25</sup>S. Guo, Z. Ya, P. Wu, and M. Wan, "A review on acoustic vortices: Generation, characterization, applications and perspectives," *J. Appl. Phys.* **132**, 210701 (2022).
- <sup>26</sup>D. Baresch, J.-L. Thomas, and R. Marchiano, "Observation of a single-beam gradient force acoustical trap for elastic particles: Acoustical tweezers," *Phys. Rev. Lett.* **116**, 024301 (2016).
- <sup>27</sup>A. Marzo, S. A. Seah, B. W. Drinkwater, D. R. Sahoo, B. Long, and S. Subramanian, "Holographic acoustic elements for manipulation of levitated objects," *Nat. Commun.* **6**, 8661 (2015).
- <sup>28</sup>N. Jiménez, V. J. Sánchez-Morcillo, R. Picó, L. M. García-Raffi, V. Romero-García, and K. Staliunas, "High-order acoustic Bessel beam generation by spiral gratings," *Phys. Procedia* **70**, 245–248 (2015).
- <sup>29</sup>M. E. Terzi, S. A. Tsypar, P. V. Yuldashev, M. M. Karzova, and O. A. Sapozhnikov, "Generation of a vortex ultrasonic beam with a phase plate with an angular dependence of the thickness," *Moscow Univ. Phys.* **72**, 61–67 (2017).
- <sup>30</sup>Y. Jin, R. Kumar, O. Poncelet, O. Mondain-Monval, and T. Brunet, "Flat acoustics with soft gradient-index metasurfaces," *Nat. Commun.* **10**, 143 (2019).
- <sup>31</sup>D.-C. Chen, Q.-X. Zhou, X.-F. Zhu, Z. Xu, and D.-J. Wu, "Focused acoustic vortex by an artificial structure with two sets of discrete Archimedean spiral slits," *Appl. Phys. Lett.* **115**, 083501 (2019).
- <sup>32</sup>J. Li, A. Crivoi, X. Peng, L. Shen, Y. Pu, Z. Fan, and S. A. Cummer, "Three dimensional acoustic tweezers with vortex streaming," *Commun. Phys.* **4**, 113 (2021).
- <sup>33</sup>X. Jiang, Y. Li, B. Liang, J.-C. Cheng, and L. Zhang, "Convert acoustic resonances to orbital angular momentum," *Phys. Rev. Lett.* **117**, 034301 (2016).
- <sup>34</sup>Z. Guo, H. Liu, H. Zhou, K. Zhou, S. Wang, F. Shen, Y. Gong, J. Gao, S. Liu, and K. Guo, "High-order acoustic vortex field generation based on a metasurface," *Phys. Rev. E* **100**, 053315 (2019).
- <sup>35</sup>Y.-R. Jia, W.-Q. Ji, D.-J. Wu, and X.-J. Liu, "Metasurface-enabled airborne fractional acoustic vortex emitter," *Appl. Phys. Lett.* **113**, 173502 (2018).
- <sup>36</sup>Y. Luo, Y. Jia, J. Yao, D. Wu, and X. Liu, "Enhanced fractional acoustic vortices by an annulus acoustic metasurface with multi-layered rings," *Adv. Mater. Technol.* **5**, 2000356 (2020).
- <sup>37</sup>H. Esfahlani, H. Lissek, and J. R. Mosig, "Generation of acoustic helical wavefronts using metasurfaces," *Phys. Rev. B* **95**, 024312 (2017).
- <sup>38</sup>C. J. Naify, C. A. Rohde, T. P. Martin, M. Nicholas, M. D. Guild, and G. J. Orris, "Generation of topologically diverse acoustic vortex beams using a compact metamaterial aperture," *Appl. Phys. Lett.* **108**, 223503 (2016).
- <sup>39</sup>C. A. Rohde and C. J. Naify, "Detecting acoustic chirality with matched metamaterial vortex wave antennas," *J. Acoust. Soc. Am.* **154**, 721–729 (2023).
- <sup>40</sup>X. Jiang, D. Ta, and W. Wang, "Modulation of orbital-angular-momentum symmetry of nondiffractive acoustic vortex beams and realization using a metasurface," *Phys. Rev. Appl.* **14**, 034014 (2020).
- <sup>41</sup>Y. Chen and G. Hu, "Broadband and high-transmission metasurface for converting underwater cylindrical waves to plane waves," *Phys. Rev. Appl.* **12**, 044046 (2019).
- <sup>42</sup>C. W. Cushing, M. J. Kelsten, X. Su, P. S. Wilson, M. R. Haberman, and A. N. Norris, "Design and characterization of a three-dimensional anisotropic additively manufactured pentamode material," *J. Acoust. Soc. Am.* **151**, 168–179 (2022).
- <sup>43</sup>H. T. O'Neil, "Theory of focusing radiators," *J. Acoust. Soc. Am.* **21**, 516–526 (1949).
- <sup>44</sup>H. Kogelnik and T. Li, "Laser beams and resonators," *Appl. Opt.* **5**, 1550–1567 (1966).
- <sup>45</sup>V. V. Kotlyar, A. A. Almazov, S. N. Khonina, V. A. Soifer, H. Elfstrom, and J. Turunen, "Generation of phase singularity through diffracting a plane or Gaussian beam by a spiral phase plate," *J. Opt. Soc. Am. A* **22**, 849–861 (2005).
- <sup>46</sup>Z. S. Sacks, D. Rozas, and G. A. Swartzlander, Jr., "Holographic formation of optical-vortex filaments," *J. Opt. Soc. Am. B* **15**, 2226–2234 (1998).
- <sup>47</sup>N. Xiao, C. Xie, E. Jia, J. Li, R. Giust, F. Courvoisier, and M. Hu, "Caustic interpretation of the abruptly autofocusing vortex beams," *Opt. Express* **29**, 19975 (2021).
- <sup>48</sup>E. A. Zabolotskaya and R. V. Khokhlov, "Quasi-plane waves in the nonlinear acoustics of confined beams," *Sov. Phys. Acoust.* **15**, 35–40 (1969).
- <sup>49</sup>G. N. Watson, *A Treatise on the Theory of Bessel Functions*, 2nd ed. (Cambridge University Press, Cambridge, UK, 1944), Sec. 2.2, Eq. (5).
- <sup>50</sup>I. S. Gradshteyn and I. M. Ryzhik, *Table of Integrals, Series, and Products*, 4th ed. (Academic, San Diego, 1965), Items 6.631–7 and 7.414–11.
- <sup>51</sup>M. F. Hamilton, "Sound beams," in *Nonlinear Acoustics*, 2nd ed., edited by M. F. Hamilton and D. T. Blackstock (Acoustical Society of America, New York, 2008), Chap. 8.
- <sup>52</sup>M. Abramowitz and I. A. Stegun, editors, *Handbook of Mathematical Functions*, 4th ed. (Dover, New York, 1972), Sec. 10.2.
- <sup>53</sup>J. E. Curtis and D. G. Grier, "Structure of optical vortices," *Phys. Rev. Lett.* **90**, 133901 (2003).
- <sup>54</sup>J. W. Goodman, *Introduction to Fourier Optics*, 3rd ed. (Roberts, Englewood, CO, 2005), Secs. 4.2.3 and 5.2.1.
- <sup>55</sup>E. G. Williams, *Fourier Acoustics* (Academic, San Diego, 1999), Sec. 2.9.
- <sup>56</sup>N. Jiménez, J. Ealo, R. D. Muelas-Hurtado, A. Duclos, and V. Romero-García, "A helicoidal parametric antenna for subwavelength vortex generation," *Proc. Mtgs. Acoust.* **48**, 045001 (2022).
- <sup>57</sup>S. Gspan, A. Meyer, S. Bernet, and M. Ritsch-Marte, "Optoacoustic generation of a helicoidal ultrasonic beam," *J. Acoust. Soc. Am.* **115**, 1142–1146 (2004).

- <sup>58</sup>C. Zhou, Q. Wang, S. Pu, Y. Li, G. Guo, H. Chu, Q. Ma, J. Tu, and D. Zhang, “Focused acoustic vortex generated by a circular array of planar sector transducers using an acoustic lens, and its application in object manipulation,” *J. Appl. Phys.* **128**, 084901 (2020).
- <sup>59</sup>D. Zhao, J.-L. Thomas, and R. Marchiano, “Generation of spherical vortex beams to trap large particles for enhanced axial force,” *Ultrasonics* **111**, 106296 (2021).
- <sup>60</sup>W.-C. Lo, C.-H. Fan, Y.-J. Ho, C.-W. Lin, and C.-K. Yeh, “Tornado-inspired acoustic vortex tweezer for trapping and manipulating micro-bubbles,” *Proc. Natl. Acad. Sci. U.S.A.* **118**, e2023188118 (2021).
- <sup>61</sup>Y. Li, P. Li, N. Ding, G. Guo, Q. Ma, J. Tu, and D. Zhang, “Weak-focused acoustic vortex generated by a focused ring array of planar transducers and its application in large-scale rotational object manipulation,” *Chin. Phys. B* **30**, 044302 (2021).
- <sup>62</sup>A. Marzo, M. Caleap, and B. W. Drinkwater, “Acoustic virtual vortices with tunable orbital angular momentum for trapping of Mie particles,” *Phys. Rev. Lett.* **120**, 044301 (2018).
- <sup>63</sup>A. D. Pierce, *Acoustics*, 3rd ed. (Springer, Cham, Switzerland, 2019), Secs. 8.2 and 8.5.
- <sup>64</sup>Y. Li, Q. Wang, G. Guo, H. Chu, Q. Ma, J. Tu, and D. Zhang, “Pulling force of acoustic-vortex beams on centered elastic spheres based on the annular transducer model,” *Chin. Phys. B* **29**, 054302 (2020).
- <sup>65</sup>R. Marchiano, F. Coulouvrat, L. Ganjehi, and J.-L. Thomas, “Numerical investigation of the properties of nonlinear acoustical vortices through weakly heterogeneous media,” *Phys. Rev. E* **77**, 016605 (2008).
- <sup>66</sup>X. Pan, J. Wu, Z. Li, C. Zhang, C. Deng, Z. Zhang, H. Wen, Q. Gao, J. Yang, Z. Yi, M. Yu, L. Liu, F. Chi, and P. Bai, “Laguerre-Gaussian mode purity of Gaussian vortex beams,” *Optik* **230**, 166320 (2021).